Title

Quantitative Scanning Transmission Electron Microscopy for Materials Science: Imaging, Diffraction, Spectroscopy, and Tomography

Journal

Annual Review of Materials Research, 53(1)

ISSN

0084-6600

Author

Ophus, Colin

Publication Date

2023-07-03

DOI

10.1146/annurev-matsci-080921-092646

ANNUAL REVIEWS

Annual Review of Materials Research

Quantitative Scanning Transmission Electron Microscopy for Materials Science: Imaging, Diffraction, Spectroscopy, and Tomography

Colin Ophus

National Center for Electron Microscopy, Molecular Foundry, Lawrence Berkeley National Laboratory, Berkeley, California, USA; email: cophus@gmail.com

Annu. Rev. Mater. Res. 2023. 53:105–41

First published as a Review in Advance on April 18, 2023

The *Annual Review of Materials Research* is online at matsci.annualreviews.org

https://doi.org/10.1146/annurev-matsci-080921-092646

Keywords

scanning transmission electron microscopy, materials science, quantitative analysis, simulation, imaging, diffraction, spectroscopy, tomography

Abstract

Scanning transmission electron microscopy (STEM) is one of the most powerful characterization tools in materials science research. Due to instrumentation developments such as highly coherent electron sources, aberration correctors, and direct electron detectors, STEM experiments can examine the structure and properties of materials at length scales of functional devices and materials down to single atoms. STEM encompasses a wide array of flexible operating modes, including imaging, diffraction, spectroscopy, and 3D tomography experiments. This review outlines many common STEM experimental methods with a focus on quantitative data analysis and simulation methods, especially those enabled by open source software. The hope is to introduce both classic and new experimental methods to materials scientists and summarize recent progress in STEM characterization. The review also discusses the strengths and weaknesses of the various STEM methodologies and briefly considers promising future directions for quantitative STEM research.

1. INTRODUCTION

1.1. Scanning Transmission Electron Microscopy

Characterization lies at the heart of materials science research. The discovery of new properties, the design and engineering of materials, the quantification of defects, and the understanding of material physics and chemistry each require robust methods to measure structure and properties over length scales from the macroscopic to the atomic. Scanning transmission electron microscopy (STEM) is one of the most powerful characterization tools employed by material scientists, in large part due to its unmatched spatial resolution and flexibility. **Figure 1** shows schematics of various STEM measurements. The components of a STEM instrument include a highly coherent electron source consisting of a tip and an anode to generate free electrons, a tube of electrodes to accelerate the electron beam to voltages of 20–300 kV (or even higher in specialized instruments), condenser lenses to define the illumination condition, scanning coils to move the beam over the sample surface, an objective lens to form converged probes, a stage to accurately position samples, and, finally, detectors to measure the distribution of the position, momentum, and/or energy of electrons scattered by the sample. A large range of detector configurations can be implemented in STEM, encompassing monolithic single- or few-pixel charge collectors (1), high-speed pixelated

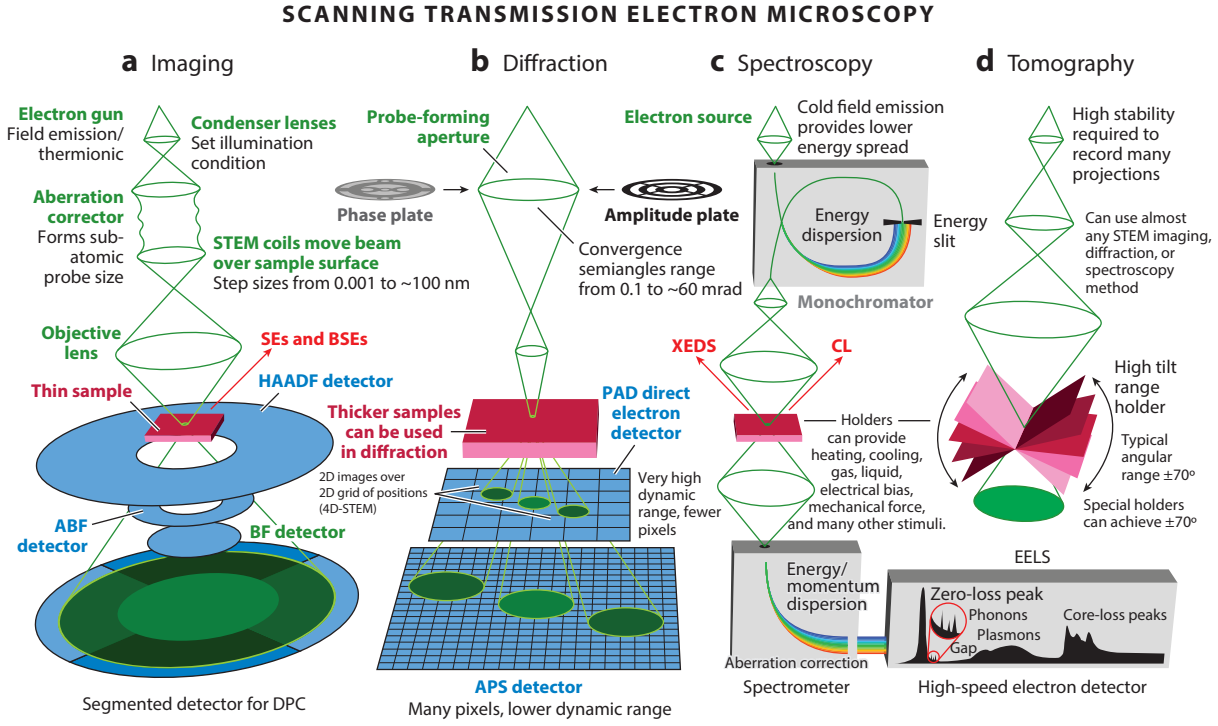

Figure 1

Characterization methods in STEM. Measurements are grouped by (*a*) imaging, (*b*) diffraction, (*c*) spectroscopy, and (*d*) tomography. However, the various methods are often combined for multimodal studies in the same instrument. This measurement flexibility makes the modern STEM instrument "a synchrotron in a microscope" (15). Abbreviations: ABF, annular bright field; APS, active pixel sensor; BF, bright field; BSEs, backscattered electrons; CL, cathodoluminescence; DPC, differential phase contrast; EELS, electron energy loss spectroscopy; HAADF, high-angle annular dark field; PAD, pixel array detector; SEs, secondary electrons; STEM, scanning transmission electron microscopy; XEDS, X-ray energy-dispersive spectroscopy.

detectors (2–4), and detectors integrated into spectrometers (5). Researchers can also use detectors optimized to collect photons and X-rays emitted by the sample due to the electron probe or backscattered and secondary electrons. A common and very important addition to modern STEM instruments is a probe aberration corrector, which can remove spherical and nonradially symmetric aberrations induced by the objective lens and other electron optics, allowing for atomic-resolution measurements (6). In addition to an aberration corrector, prespecimen optical elements such as monochromators (7), phase plates (8–12), amplitude plates (13), and electrostatic or electromagnetic beam blankers (14) may be used to modify the electron beam incident on the sample. Sample holders also dramatically increase the measurement phase space of STEM, especially for in situ experiments. This amazing degree of characterization flexibility truly makes STEM, to quote Brown (15), "a synchrotron in a microscope" (16).

This review article focuses on the quantitative application of STEM to materials science studies for imaging, diffraction, spectroscopy, and tomography. It primarily covers recent progress in STEM experiments, analysis, and simulation. STEM instrumentation development has a long and rich history, which is not covered here. Instead, readers are directed to the excellent review article published by Liu (17). It also does not discuss conventional transmission electron microscopy (TEM) experiments, as STEM has overtaken TEM in materials science research and is even making inroads into biological studies and the imaging of soft matter. Many good resources for quantitative TEM can be found in the literature (e.g., 18). The hope is that this article can introduce STEM characterization methods to material scientists who may not be familiar with the extremely wide breadth of characterization possibilities in STEM.

1.2. What Can STEM Measure?

I have divided STEM measurements into four broad categories, shown schematically in **Figure 1**: imaging, diffraction, spectroscopy, and tomography. The techniques shown are nonexhaustive, and many measurements blur the lines between these categories, including diffractive imaging methods such as ptychography, position-resolved spectroscopic imaging, and momentum-energy characterization. Nevertheless, this review is divided into these four broad topics. Modern STEM imaging experiments typically utilize multiple simultaneous detectors in a far-field diffraction plane, as shown in **Figure 1*a***, including annular dark field (ADF), high-angle ADF (HAADF), bright field (BF), annular bright field (ABF), and segmented detectors for differential phase contrast (DPC) (19). Despite the measurements taking place in a diffraction plane, the resulting signals are 2D images (or 1D line traces) where each pixel corresponds to a different probe position on the sample surface. In STEM instruments with probe aberration correction, the convergence semiangle can be opened up to tens of milliradians, producing converged probes smaller than 1 Å, which are able to resolve individual atoms and atomic columns. Atomic-resolution STEM imaging is most commonly used to measure the atomic 2D position (and in many cases the atomic species) in crystalline materials, including the configuration of dopants, defects, and surfaces. HAADF imaging is best suited for measuring heavy elements, while BF, ABF, and DPC are able to measure positions of light elements. STEM is also able to image materials at intermediate and low magnifications, which is often important for placing atomic-resolution images in the proper environmental context for materials and devices. STEM imaging has been reviewed by Liu (17).

Figure 1*b* shows the essence of a STEM diffraction experiment. In contrast to an imaging experiment, a STEM diffraction experiment uses a pixelated detector to record an image of the diffracted probe after scattering from the sample. For a single-probe position, these experiments are known as convergent beam electron diffraction (CBED), microdiffraction, or nanodiffraction experiments. These diffraction patterns can also be measured as a function of the probe position in experiments known as 4D-STEM, nanobeam electron diffraction (NBED), scanning electron

nanodiffraction (SEND), and various other related names (20). These experiments can use small convergence angles to produce spot patterns that resemble traditional TEM diffraction experiments, intermediate convergence angles (and thus a smaller probe on the sample surface) to boost the spatial resolution, or large convergence angles to generate coherent interference in the diffraction patterns. Microdiffraction is covered in detail in the textbook by Spence & Zuo (21), and 4D-STEM development has been reviewed by Ophus (22).

Figure 1*c* shows the typical configuration of a spectroscopic STEM experiment. We can characterize the energy distribution of electrons after inelastic scattering using electron energy loss spectroscopy (EELS), the energies of emitted X-rays using a method named X-ray energy-dispersive spectroscopy (XEDS), or light generation using cathodoluminescence (CL). Spectroscopic STEM experiments often benefit from reducing the initial energy distribution of the electron beam, using a low-energy-spread cold field emission source (23), an electron monochromator (7), or both. EELS and XEDS signals can be recorded simultaneously, and both are usually recorded as a function of the probe position, producing 2D maps of atomic species. STEM-EELS can also map variations in a sample's electronic state using spectral features sometimes referred to as electron energy loss near edge structures (24), which can be calculated from first principles (25). Electron spectrometers have become quite advanced and are able to correct aberrations to a high order and measure a large range of energy losses (5). These advances have allowed for detailed mapping of spectral features such as bonding signals from core-loss excitations or variations in local plasmons, phonons, or band gap signals. A detailed description of EELS can be found in Egerton's (24) textbook. A review of XEDS methods is also available (26), as is a review of CL in STEM (27).

Figure 1*d* shows a schematic of a STEM tomography experiment, where imaging, diffraction, or spectroscopy experiments are carried out for different sample tilts. By using computational methods, we can reconstruct the sample's structure or measure material properties resolved in three dimensions. There are a large number of computational algorithms that can reconstruct 3D volumes from 2D projections. Common noniterative tomographic reconstruction methods include filtered or weighted back-projection and Fourier interpolation methods. Iterative reconstruction algorithms are more common in STEM tomography as they generally produce higher-quality reconstructions. Many reviews of STEM tomography can be found in the literature (e.g., 28–30).

1.3. Quantitative Computational Analysis

Quantitative STEM experiments are possible primarily due to our ability to use computers to analyze their measurements. Computer control is also important for controlling STEM experiments (31), especially for modern aberration correction. Early STEM detectors consisted of a scintillator connected to a photomultiplier. Once computers became widely available, STEM was transformed into a digital science. Electronic detector signals were recorded on magnetic tape, and then computer algorithms could be applied offline (postexperiment) to perform quantitative measurement. Spectroscopic and 3D tomographic STEM experiments require more storage space and more computer memory to analyze than images, but rapidly falling costs quickly made digital analysis of these signals feasible, both online and offline (32). Analysis of large-scale diffraction experiments, such as those using 4D-STEM, requires still more storage space and memory but is now possible on personal computers or even powerful laptops (4, 33). Currently, much of the data analysis in STEM is performed using closed source tools developed by researchers. This situation is rapidly changing, however, with the proliferation of open source codes in all scientific fields (34) and widespread adoption of findable, accessible, interoperable, and reusable (FAIR) principles for data (35). These analysis tools are written in programming languages including FORTRAN, C,

C++, Java, JavaScript, MATLAB, and Python. Python in particular is becoming the language of choice for scientific analysis, driven by the popular NumPy and SciPy packages and the explosive growth of machine learning in science in general, including in STEM research (36).

There is currently a large number of user-written analysis codes for STEM data. One of the largest collections of tools for imaging analysis uses the built-in tools and plug-ins written for the open source Java program ImageJ. Many useful ImageJ tools have been applied to STEM studies (e.g., 37). Likely the most widespread open source Python analysis toolkit for STEM is HyperSpy (38). HyperSpy was initially geared toward analysis of spectral data such as those from EELS or XEDS but has been expanded with many application-specific analysis tools for image analysis such as AtomMap (39), TopoTEM (40), ParticleSpy (41), 4D-STEM analysis in pyxem (42), Diffsims (43), orix (44), and file input/output with Rosettasciio. Large Python open source projects for 4D-STEM analysis include LiberTEM (45) and py4DSTEM (33) with analysis modules such as crystal orientation mapping (46). Other Python tools for analysis of imaging and diffraction data include STEMTooL (47) and pycroscopy (48) with the associated machine learning toolkit AtomAI (49). There are multiple popular open source tomography codes, including TomoPy (50), ASTRA (51), TomViz (52), and IMOD (53).

Instrument vendors often also provide software that is capable of both controlling experiments and performing analysis. These include Gatan's DigitalMicrograph/Gatan Microscopy Suite, Nion Swift, Thermo Fisher's Velox, the Amira 3D toolkit, JEOL's PyJEM, and Bruker's ESPRIT. DigitalMicrograph has a robust library of vendor- and user-provided plug-ins to perform various experiments and analyses (54). DigitalMicrograph now supports Python scripting, while Nion Swift allows users to directly program both experiments and analysis in Python and is itself written in Python. In the future, we expect that all microscopy vendors will both allow user access to all microscope components using programmatic control and provide the option to save and load data into open source formats.

One set of experimental processing methods that is specific to STEM and other scanning probe methods is drift correction. Because STEM pixels are measured serially, the sample can move during scanning or charge buildup, and other electronic instabilities can lead to displacement of the probe with respect to the target position. Several authors have created drift correction methods, including nonrigid or nonlinear ones such as SmartAlign by Jones et al. (55) and SPmerge by Ophus et al. (56). Other authors have implemented various drift correction algorithms for different STEM modalities (57–59).

It is strongly recommended that any STEM researcher who is serious about data analysis learn at least one programming language. No matter how good open source tools become, new STEM experiments and methods are being designed that require new analysis or simulation methods. In addition to the various textbooks already mentioned, we recommend Kirkland's (60) textbook for the best mathematical and programmatic introduction to STEM. This book covers many key topics in the mathematical modeling of microscopy such as the fast Fourier transform, sampling and antialiasing, potential parameterization, and numerical methods to solve partial differential equations. With knowledge of these topics, researchers will find it much easier to use and adapt existing open source analysis codes, as well as to design their own. Given its ease of use, large online community, large existing codebase, and the prevalence of machine learning in scientific research, Python is almost certainly the best choice for most researchers.

1.4. Quantitative STEM Simulations

Another bedrock concept for quantitative STEM studies is the use of simulations to model both elastic and inelastic scattering. These simulations are used to help with both experimental design

and the interpretation of complex data sets. Free electrons traveling from the electron source through the electromagnetic fields created by electron optics are the easiest to model using the single-particle ray-optics picture. However, to accurately model the near-field interaction of free electrons with atoms in a condensed matter sample, we must compute the evolution of their quantum-mechanical wave functions. These calculations can be performed using the nonrelativistic Schrödinger equation, the relativistic Dirac equation, or, most commonly, a relativistically corrected electron wavelength and mass as an approximation in the Schrödinger equation. Unfortunately, unless we assume infinitesimal sample thickness, the Schrödinger equation for fast electrons contains noncommuting operators and therefore must be solved numerically (60).

There are two long-established algorithms to model elastic scattering in TEM experiments. The first is known as the Bloch-wave method, which uses a scattering matrix (S-matrix) formalism to solve for the reciprocal-space eigenstates inside the sample (60). Once these eigenstates are known, any elastic scattering TEM experiment can be modeled by solving for the coefficients of the incident wave function, propagating through the sample with matrix multiplication, and then applying the output microscope transfer function and detector operator. The Bloch-wave method is used primarily for simulations of single-unit-cell crystalline samples as the calculation time greatly increases with increasing sample size and the number of electron scattering vectors (usually called beams).

STEM experiments are far more commonly modeled with the second algorithm, named the multislice method, introduced by Cowley & Moodie (61). The multislice method is shown schematically in **Figure 2*a***. First, the sample is sliced along the beam direction into slabs thin enough to be well approximated by the single scattering approximation (the kinematical limit), typically 1–2 Å. Next, the projected potential inside each slice is computed, usually from lookup tables of the individual atomic species, in a method named the independent atom model (IAM) (60, 63). At this stage, one can also add in any additional electrics of magnetic field–induced phase shifts (64). The incident electron wave function, typically an Airy disk function, is then initialized, combined with coherent wave aberrations (60), and propagated through the sample by alternating between transmission through each slice and free-space propagation to reach the next slice. Finally, a detector function is applied to the complex exit wave, and the output intensity is calculated as the wave function amplitude squared.

The multislice method has been implemented for STEM in a large number of open source simulation codes including abTEM (65), Prismatic (70), μSTEM (71), MULTEM (72), and Dr. Probe (73). The most common method for including the effects of thermal vibration in multislice simulations is the frozen phonon method, where atoms are randomly displaced to a frozen configuration, which simulates the thermal displacements seen by a beam of fast electrons (60). The simulation outputs for different random configurations are summed incoherently until convergence. An equivalent derivation for this method known as the quantum excitation of phonons (QEP) model has also been published (74). Many STEM characterization studies of crystalline materials perform imaging or diffraction along low-index zone axes, that is, with the atomic columns aligned to the electron beam. This leads to channeling, which refers to the electron beam being focused along atomic columns, causing differences in beam propagation when the electron beam is aligned to a low-index zone axis relative to when it is tilted off-zone, and thus it can require simulations to quantitatively interpret the results (60).

The multislice method is highly flexible when simulating STEM experiments and can produce high accuracy, but it can require extremely high computation times as each individual probe position requires a separate simulation. We can reuse potential slices, crop around the probe's real space extent, or use graphics processing unit (GPU) resources for moderate calculation time reduction, but simulating large field-of-view experiments with multislice can still require hundreds

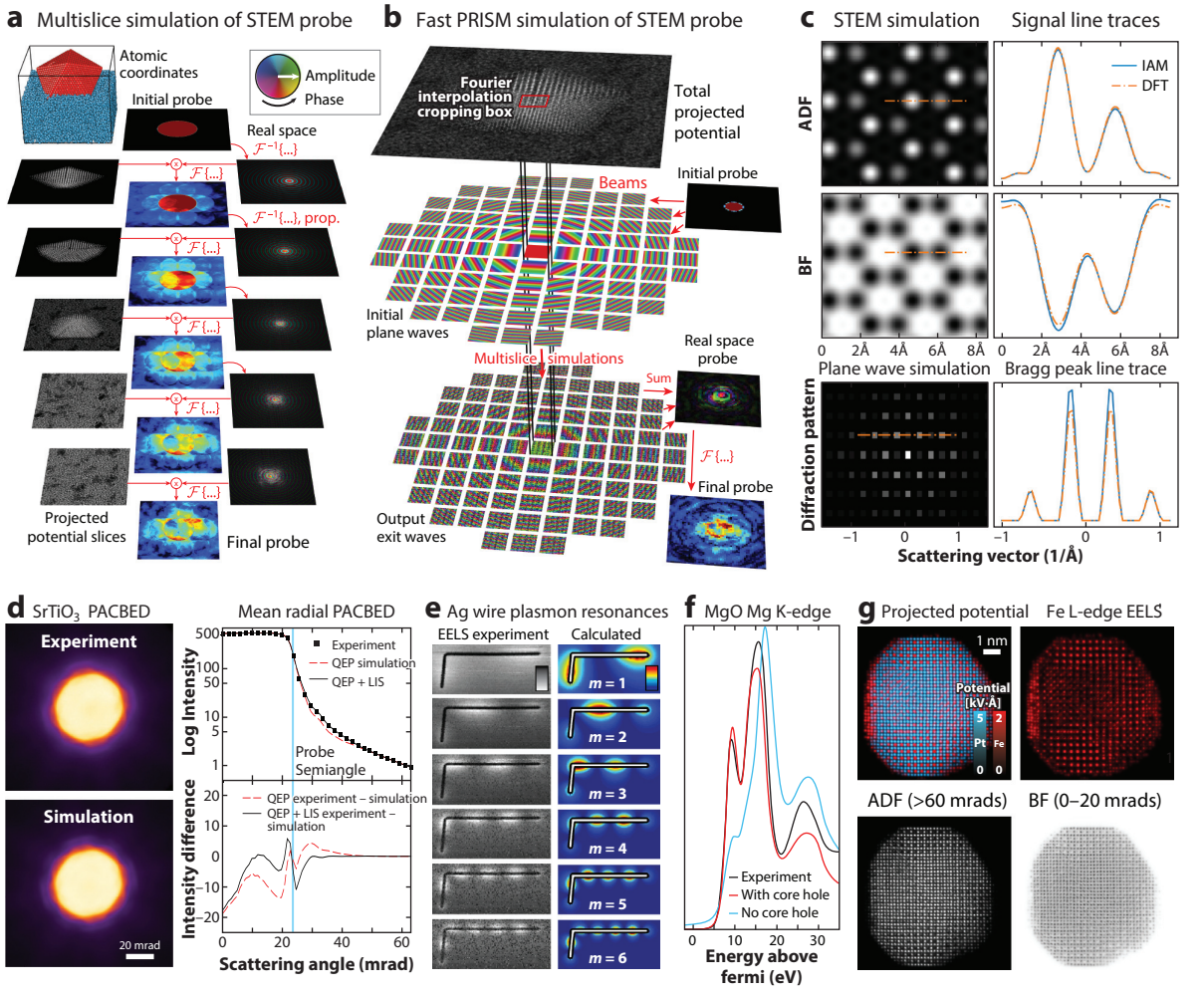

Figure 2

Annular dark field imaging in STEM. (*a*) The multislice algorithm consisting of alternating steps of transmission through a potential slice and free-space propagation. Panel adapted from Reference 62 (CC BY 4.0). (*b*) The PRISM algorithm where multislice simulations are used to construct a scattering matrix, which is then multiplied by the initial STEM probe to calculate the output probe. Panel adapted from Reference 62 (CC BY 4.0). (*c*) STEM imaging and electron diffraction simulations of hexagonal BN, comparing potential calculations using the IAM with those using DFT. Panel adapted from Reference 65 (CC BY 4.0). (*d*) PACBED experiment compared with simulation, including only thermal scattering or both thermal effects and low-loss inelastic scattering. Panel adapted with permission from Reference 66; copyright 2020 American Physical Society. (*e*) Plasmonic response of bent silver nanowires measured with EELS compared with simulations. Panel adapted with permission from Reference 67; copyright 2013 American Physical Society. (*f*) DFT calculation of the Mg K-edge in MgO, both with and without core-hole effects included. Panel adapted from Reference 68 with permission from Elsevier. (*g*) Simulation of Fe L-edge intensity in an FePt NP, where elastic scattering is calculated before and after the core-loss event using PRISM. Panel adapted from Reference 69 (CC BY 4.0). Abbreviations: ADF, annular dark field; BF, bright field; BN, boron nitride; DFT, density-functional theory; EELS, electron energy loss spectroscopy; IAM, independent atom model; LIS, low-loss inelastic scattering; NP, nanoparticle; PACBED, position-averaged convergent beam electron diffraction; PRISM, plane-wave reciprocal-space interpolated scattering matrix; QEP, quantum excitation of phonons; STEM, scanning transmission electron microscopy.

or even thousands of central processing unit or GPU hours for large simulation cells (75). To address this limitation, Ophus proposed the plane-wave reciprocal-space interpolated S-matrix (PRISM) algorithm (76). The PRISM algorithm is shown schematically in **Figure 2*b***. The projected potentials are calculated in the same manner as before, but instead of performing a multislice simulation for each probe position, we instead use plane-wave multislice simulations to calculate the rows of an S-matrix. If the STEM probe is significantly smaller than the simulation cell size, we can use Fourier interpolation to calculate every fth periodic plane wave, which corresponds to cropping the boundaries of the probe in real space. Once the S-matrix has been fully calculated, output STEM probe intensities can be computed with a speedup proportional to f^2 and f^4 for the S-matrix construction and probe multiplication steps, respectively, potentially giving large reductions in calculation times at the cost of some accuracy (76). If $f = 1$, PRISM simulations produce identical outputs to the multislice algorithm. Several open source codes have implemented the PRISM method for STEM simulations (65, 70).

As discussed above, a common approximation in STEM simulations is to independently add the parameterized atomic potentials for all species present to estimate the total projected potential (60). However, if there is a significant change in the sample's electron density due to bonding (relative to the IAM), this will in turn modify the screening of the ionic cores and therefore the projected potential. A more accurate method of calculating the projected potentials is to use density-functional theory (DFT) to compute a more accurate charge distribution. The abTEM simulation code directly links DFT calculations using the GPAW code to electron scattering simulations (65), as demonstrated in **Figure 2*c*** for simulations of hexagonal boron nitride (h-BN). In the ADF simulation, we see essentially no difference between IAM- and DFT-derived potentials. However, both the BF and diffraction pattern simulations show a significant discrepancy between IAM and DFT potentials, with the latter presumed to be more accurate.

All of the previous simulations discussed were for elastic scattering. However, virtually all STEM experiments also include a significant amount of inelastic scattering (64). The inelastic scattering events that can be measured using EELS can include negligible energy changes such as phonon scattering, energy changes of 10–50 eV such as in surface or bulk plasmons, large energy changes (from 50 up to thousands of electron volts) due to core-loss scattering, and other inelastic interactions (19). **Figure 2*d*** compares a position-averaged CBED (PACBED) experiment and a simulation from Reference 66. While the intensities appear quite similar, performing a radial average shows that to get quantitative agreement, the inelastic plasmon energy loss must be included, which in this case was implemented using a Monte Carlo algorithm proposed by Mendis (77). The spatial distribution of plasmon losses can also be measured and simulated, shown, for example, in **Figure 2*e*** from Reference 67. Here the authors used boundary-element-method modeling of Maxwell's equations to compute the distribution of plasmonic resonant modes, with good quantitative agreement with experiment.

Figure 2*f* shows an EELS simulation of the Mg K-edge from an MgO DFT simulation, with and without including core-hole effects, compared with an experiment (68). Core-hole simulations require larger simulation supercells and therefore much longer calculation times, but as this example shows, they are often necessary for accurate simulation of core-loss EELS. Another approach to the quantification of inelastic core-loss EELS is to perform semiempirical simulations that combine atomic multiplet, crystal field, and charge transfer theories. This approach can include some effects difficult to model with DFT calculations and has a much lower computational burden. Finally, some of the most computationally intensive simulations are those that combine both elastic and inelastic calculations. Dwyer (78) showed how core-loss inelastic scattering events can be incorporated into multislice simulations, which is important for quantitative simulation of samples thick enough for elastic scattering to strongly modulate inelastic scattering. **Figure 2*g***

shows a so-called double-channeling simulation of an FePt nanoparticle (NP) where the sample is thick enough that there may be significant elastic scattering both before and after inelastic transitions. The sharp contrast variations in the Fe columns visible in the Fe L-edge intensity are due to the elastic scattering. Computing all of these possible scattering pathways is not feasible using the conventional multislice approach. To address this limitation, Brown et al. (69) demonstrated a modification of the PRISM algorithm to perform these calculations on large simulation cells.

There has also been progress in quantitative simulations of other spectroscopic methods in STEM. Zeiger & Rusz (79) have recently introduced a method to simulate these vibrational spectra by combining molecular dynamics and a δ thermostat with multislice simulations. Quantitative simulation of XEDS has been investigated by various researchers (80, 81), and Yamamoto et al. (82) have derived a model of light emission induced by fast electrons to simulate CL experiments. Details on inelastic scattering modeling have been given in References 71 and 78.

1.5. Limitations of STEM Characterization

STEM is a powerful and flexible characterization tool, but it cannot be used to measure the structure and properties of all samples. One of the primary limitations of STEM is that samples must be thin enough to be transparent to the electron beam. STEM experiments are somewhat less restrictive than plane-wave TEM studies, often producing interpretable signals over a wider thickness range. Even though the scattering angles in high-voltage STEM are small, if the sample is thicker than several mean free paths it can be difficult (though not impossible) to measure material properties. With specialized high-voltage STEM instruments ($\geq$1 MeV), samples with thicknesses up to tens of micrometers can be imaged. However, quantitative STEM measurements typically require that the maximum thickness be on the order of 0.2 to 0.5 (depending on the specific measurement) times the electron mean free path in the sample (83). The elastic mean free path of most materials ranges from approximately 50 nm/ρ for 20-kV, 200 nm/ρ for 100-kV, and 400 nm/ρ for 300-kV electrons, where ρ is the sample density in grams per cubic centimeter (84). The inelastic mean free path of materials covers a similar range of about 50–200 nm for most samples. Thus, performing STEM experiments with the highest spatial, angular, and spectroscopic resolution often requires sample thicknesses to be <20 nm. This is one of the reasons why STEM studies of 2D materials are so prevalent. Recent progress in the preparation of thin samples other than 2D materials for STEM experiments is largely driven by improvements in focused ion beam (FIB) technology. FIB sample preparation has been reviewed by Zhang et al. (85) and others.

Assuming a thin sample can be produced, the limiting factor of most STEM experiments is the damage to the sample induced by the electron beam. Electron beam damage mechanisms include large momentum transfer from the beam to the sample atoms (known as knock-on damage), radiolysis caused by ionization, and electrostatic charging. Knock-on damage is the dominant mechanism for conductive samples, while radiolysis and charging damage are more common for insulating samples (86). Minimizing beam damage is primarily accomplished by reducing the electron dose, though it can also be achieved with creative scanning strategies (87) or chemical modification of the sample (88). Other limitations are the sample's ability to tolerate the low-pressure vacuum environment and the cleanliness of the microscope environment. Both the microscope and the sample must be relatively free of hydrocarbons and other organic molecules to prevent contamination (86). Contamination in STEM typically results in hydrocarbons being polymerized by the STEM beam, leading to a steady buildup of carbon in the field of view, which in turn obscures the measurements. Common mitigation strategies for contamination include sample heating, cleaning the specimen with plasma, electron beam showering, and improved microscope vacuum.

2. IMAGING

In STEM imaging, the focused electron probe is moved across the sample surface using scanning coils, which are typically a pair of in-plane electromagnetic coils positioned along orthogonal directions to allow for full 2D motion of the beam. A typical STEM imaging example will record a 2D grid of probe positions, forming a 2D image from each of the single-pixel detectors. The step size between adjacent STEM probes can be set independently of the probe size, allowing for extremely large fields of view if needed (89). We must take care when interpreting images generated from experiments with a much smaller probe size than step size, as in some cases this can produce aliasing artifacts (70). However, these potential artifacts can be made useful when scanning beam-sensitive crystalline samples by using a step size slightly larger than an integer multiple of the crystalline unit-cell dimensions to form moiré images of the crystal or its strain field (90). As discussed above, slower scanning usually requires postprocessing to correct sample- and charging-induced drift artifacts (55, 56, 58).

After scattering from the sample, electron intensities are measured in the far field, typically with monolithic single-pixel detectors that span a fixed annular range. Unlike diffraction, spectroscopy, or tomography experiments, STEM images can be recorded very quickly and can often be interpreted immediately. In a typical STEM experiment, many images of the sample will be recorded at low, intermediate, and high magnification using a variety of imaging modes. Multiscale imaging is often important for positioning high-resolution measurements in the proper material structural context of the sample. Often, the STEM operator will perform basic analysis of images during the experiment, such as line trace comparisons, numerical Fourier transforms, or geometric phase analysis of crystalline lattices. Various STEM detectors can be used simultaneously, often providing complementary information about the sample being measured. Gauquelin et al. (91) have compared different STEM imaging modes.

2.1. Annular Dark Field

ADF (and especially HAADF) is by a fair margin the most popular imaging mode in STEM. The primary reasons are that incoherent HAADF signals are straightforward to collect, have a well-understood approximate dependence on atomic number $Z^{1.3}$–Z^2 (92), are fairly robust to thick or defected samples, and have better intrinsic resolution than coherent signals and are easier to interpret. The Z dependence of the signal is why HAADF-STEM is often referred to as Z-contrast STEM (19). By "easier to interpret," I mean that HAADF images are approximately linearly correlated (or at least monotonically varying) with the underlying sample potential—these images are essentially a direct measurement of the sample with some blurring given by convolution with the probe size in the sample plane. Additionally, ADF imaging can be performed simultaneously with the various other imaging modes described below. Given that many interesting samples are complex and relatively thick and contain strongly scattered elements, HAADF-STEM is an excellent tool to characterize materials from the micrometer scale down to the atomic scale.

The ultimate sensitivity limit for STEM is the detection of single atoms, which was achieved experimentally for U and Th atoms in 1970 by Crewe et al. (93). With further STEM instrumentation improvements, various researchers incorporated few- or single-atom imaging into materials science studies (e.g., 94, 95). Allen et al. (96) used HAADF-STEM to localize single Au atoms in an Si nanowire, shown in **Figure 3*a***. By recording a focal series of HAADF images, they were able to determine the 3D position of Au atoms both along a twin boundary and in the bulk nanowire, establishing the presence of these bulk impurities far above the estimated solubility limit of Au in Si. Single-atom STEM imaging progress was reviewed by Colliex et al. (97).

In order to perform quantitative HAADF measurements, we must normalize the measured signal as proposed by Singhal et al. (94). LeBeau et al. (104) proposed an absolute quantification

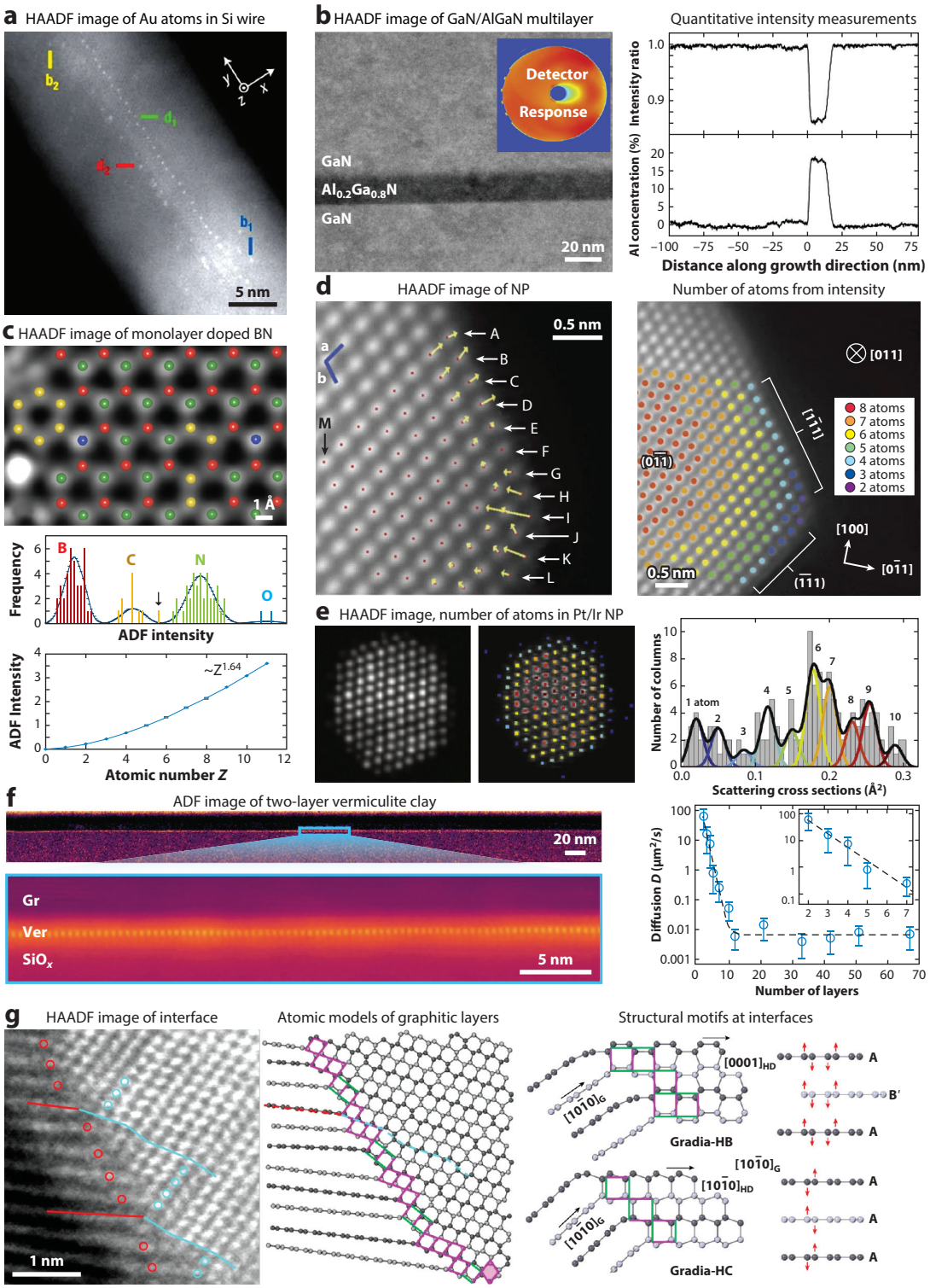

(Caption appears on following page)

Figure 3 (*Figure appears on preceding page*)

ADF imaging in STEM. (*a*) Single Au atoms trapped at a twin boundary (d_1, d_2) and in the Si nanowire bulk (b_1, b_2). Panel adapted from Reference 96 with permission from Springer Nature. (*b*) Epitaxial multilayer (*left*), with the inset showing the measured detector response. The calibrated intensity and composition measurement are shown on the right. Panel adapted from Reference 98 with permission from Elsevier. (*c*) Smoothed image showing atomic positions and species (*top*) and the power law of intensities (*bottom*). Panel adapted from Reference 99 with permission from Springer Nature. (*d*) Average of 56 HAADF images of a Pt NP after nonrigid registration (*left*) with positions and intensity-derived atomic column thicknesses (*right*). Panel adapted from Reference 100 with permission from Springer Nature. (*e*) Fitted model image of a Pt/Ir NP (*left*) with intensity-derived atomic column thicknesses. Panel adapted from Reference 101 with permission from Elsevier. (*f*) Image of two clay layers showing ion positions (*left*) and measured ion diffusion for *N* layers (*right*). Panel adapted from Reference 102 with permission from Springer Nature. (*g*) Coherent interface between graphite and diamond (*left*) with the structure overlaid (*right*). Panel adapted from Reference 103 (CC BY 4.0). Abbreviations: ADF, annular dark field; BN, boron nitride; Gr, graphene; HAADF, high-angle ADF; NP, nanoparticle; STEM, scanning transmission electron microscopy; Ver, vermiculite.

method, which they demonstrated allows for nearly perfect agreement between experiment and simulation for $SrTiO_3$ samples up to 120 nm in thickness. **Figure 3*b*** shows a HAADF image of an $Al_{0.2}Ga_{0.8}N$ epitaxial layer embedded in GaN, with the detector response function shown in the inset, measured by Rosenauer et al. (98). By calibrating the measured HAADF signal on an absolute scale, they were able to precisely measure the Al composition as a function of distance and estimate a sample thickness of approximately 130 nm. On the other extreme of sample thickness, Krivanek et al. (99) demonstrated the ability to determine atomic species from a HAADF image of a monolayer BN sample doped by C and O, shown in **Figure 3*c***. They were able to identify the species of nearly each individual atom with high certainty and found that the intensity as a function of atomic number Z varied as $Z^{1.64}$, in good agreement with the model derived by Hartel et al. (105), which suggested a dependence of $Z^{1.6}$ to $Z^{1.9}$.

Figure 3*d* demonstrates quantitative measurements of a Pt NP at atomic resolution, performed by Yankovich et al. (100). By averaging many images to boost the signal-to-noise ratio, they were able to both achieve subpicometer precision for the 2D position of the atomic columns and count the number of atoms in each column. Being able to perform such precise measurements is important when analyzing the surface of catalytic NPs. **Figure 3*e*** shows a HAADF image and model fitting of a Pt/Ir catalyst NP, where De Backer et al. (101) examined the reliability of thickness quantification at low electron doses. They found that the imaging conditions for each instrument and material system must be tuned individually to optimize the trade-off between measurement reliability and damage induced by the electron beam.

Intermediate- and atomic-resolution imaging is also useful for studying dynamic processes such as diffusion. Studies of diffusion can benefit from the chemical sensitivity and better robustness against thick samples of STEM. Shi et al. (106) have reviewed in situ nanocrystal formation imaging with both TEM and STEM. **Figure 3*f*** shows a low- and high-magnification cross-sectional image of vermiculite, a hydrated clay mineral, where Cs^+ ions are intercalated between two clay layers, from Zou et al. (102). By measuring the diffusion coefficient from many samples with different numbers of layers, they found constant diffusivity for a large number of layers and an exponentially increasing diffusion for a decreasing number of layers below seven, which they attribute to thickness-dependent swelling that increases for decreasing layer numbers. STEM can also be used to tackle longstanding materials science problems. For example, Luo et al. (103) have used HAADF-STEM to image a coherent interface between graphite and diamond, shown in **Figure 3*g*** along with the associated model of the interface. They identified four different structural motifs for these coherent interfaces and proposed a model for the coherent transformation. These examples demonstrate why HAADF-STEM is a powerful tool for the characterization of materials.

2.2. Bright Field and Annular Bright Field

While (HA)ADF-STEM is very useful for imaging materials, it has several weaknesses. Using a large inner detector angle in ADF produces more interpretable contrast as the lower-angle coherent diffraction contributions are removed, but fewer electrons are collected, leading to a noisier signal. For thin specimens only a small fraction of the probe electrons will reach the detector, making this imaging mode relatively inefficient. It is difficult to directly observe and identify the species of low–atomic number elements such as C, N, or O using ADF, let alone important elements such as Li or H. One method to boost contrast in ADF imaging is to reduce the inner detector angle, producing medium-angle ADF or low-angle ADF images. An alternative imaging mode is to place the detector inside the probe convergence semiangle, collecting all or some fraction of the unscattered electrons. BF imaging in STEM typically refers to a circular detector that covers the full unscattered beam. Similar to other phase contrast imaging modes, using a small defocus will enhance the BF image contrast. Using a large probe convergence semiangle and a larger BF detector collection angle will record a large fraction of the electron beam but also produce oscillating contrast with thickness or scattering cross section, similar to plane-wave TEM imaging modes. This contrast can be very accurately modeled, as demonstrated by LeBeau et al. (107) for BF imaging of $SrTiO_3$, shown in **Figure 4*a***. They used absolute intensity measurements and quantitative multislice simulations to accurately fit both thickness and defocus, showing that BF imaging had high sensitivity and the measured intensities could be modeled with high precision.

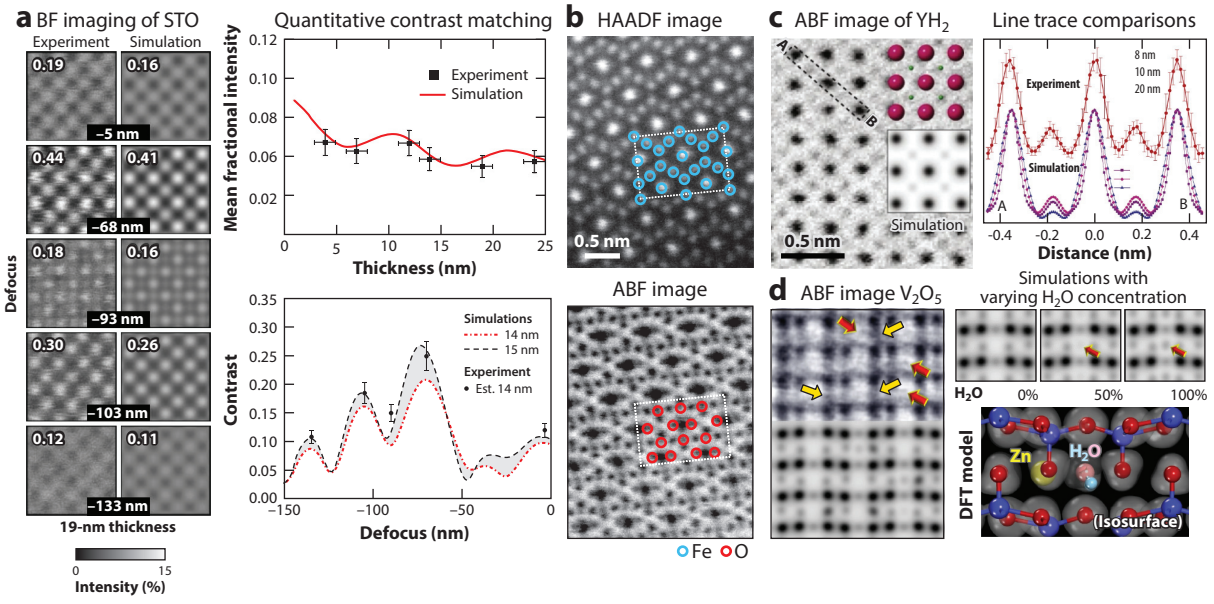

Figure 4

BF imaging in STEM. (*a*) BF imaging of STO at five defocus values, with simulation results shown adjacently. Quantitative matching of the image contrast is also shown. Panel adapted with permission from Reference 107; copyright 2009 American Physical Society. (*b*) HAADF and ABF images of Fe_3O_4 with Fe and O sites overlaid. Panel adapted from Reference 108 with permission from Oxford University Press. (*c*) ABF imaging of YH_2, with the atomic structure overlaid (Y shown in *magenta* and H in *green*) and simulation results in the inset. Line traces of experimental and simulated ABF images at three thicknesses are shown. Panel adapted from Reference 109 with permission from Springer Nature. (*d*) Intercalation of H_2O (*red arrows*) and Zn (*yellow arrows*) into a V_2O_5 cathode with simulations of varying H_2O concentration and a DFT atomic model. Panel adapted from Reference 110 (CC BY 4.0). Abbreviations: ABF, annular bright field; BF, bright field; DFT, density-functional theory; HAADF, high-angle annular dark field; STEM, scanning transmission electron microscopy; STO, $SrTiO_3$.

Okunishi et al. (108) proposed an improvement to BF-STEM where electrons are recorded from approximately half the radius of the illumination aperture out to its outer edge; they suggested that this ABF imaging mode, analogously to hollow-cone illumination in TEM, would improve contrast, reduce thickness oscillations, and allow both light and heavy elements to be imaged simultaneously. **Figure 4*b*** shows one of their results for Fe_3O_4, where the HAADF image shows only Fe columns, but in the ABF image, O columns are also visible. ABF-STEM imaging has pushed light element imaging far enough to directly locate H columns, as demonstrated by Ishikawa et al. (109), who imaged YH_2, as shown in **Figure 4*c***. They also used multislice simulations to both support their conclusions and estimate the sample thickness using the relative contrast of the Y and H columns. Direct observations of H columns were also reported by Findlay et al. (111), though their detector configuration also included dark field scattering. These observations demonstrated that ABF-STEM was a practical method to image virtually any material, though with somewhat stricter limits for quantitative imaging on sample thickness, sample tilt, and defocus relative to incoherent HAADF imaging due to phase contrast effects. ABF imaging is now very common in STEM studies of materials, used by Byeon et al. (110), for example, to study the intercalation of Zn and H_2O into a V_2O_5 cathode, as shown in **Figure 4*d***. By combining ABF imaging with DFT modeling and multislice simulations, they were able to quantify the degree of intercalation and identify multiple intermediate phases invisible to macroscopic diffraction methods.

2.3. Differential Phase Contrast

BF and ABF are imperfect phase contrast measurements due to their complicated contrast transfer functions. Almost 50 years ago, Dekkers & De Lang (112) proposed that phase contrast signals could be efficiently measured by using segmented detectors to measure the deflection of the STEM probe, an imaging method called DPC. Rose (113) had previously derived the linear relationship between probe deflection and the gradient of the projected sample potential (i.e., the sample's internal electric field), making DPC a highly efficient method to measure sample potential. DPC measurements are also sensitive to electromagnetic fields as, within electron optics, these fields produce a spatially varying deflection of the beam in an electron microscope. Because DPC signals are proportional to the gradient of the sample potential, we can approximately reconstruct this potential by performing numerical integration, which can be efficiently computed with Fourier transforms (33). We can also improve DPC measurements of the probe deflection by replacing segmented detectors with fast, pixelated direct electron detectors; this technique is referred to as center-of-mass (CoM)-DPC measurements (114). Sample potential reconstruction via integration is sometimes referred to as integrated DPC or integrated CoM (115). In general, DPC imaging can be made quantitative and can produce interpretable images for thicker specimens than conventional TEM phase contrast imaging can but is not as robust to thickness as HAADF imaging.

The first demonstration of atomic-resolution DPC was published by Shibata et al. (116), who measured the position of all atomic species and thus the polarization directions in $BaTiO_3$. **Figure 5*a*** shows an example of DPC-STEM where Han et al. (117) performed STEM experiments to characterize antiferrodistortive grain boundaries (GBs) in $SrTiO_3$. Unlike in the HAADF images, the O atomic columns are clearly visible in the DPC image, and their positions can be fit to high precision. These direct measurements of the Ti–O octahedra rotations confirmed the presence of the antiferrodistortive GB, helping to explain the transport and optical properties of $SrTiO_3$ (117). In addition to being sensitive to weakly scattering elements, DPC imaging is also very dose efficient, as shown by Shen et al. (118) in DPC images of zeolite ZSM-5 with and without single pyridine molecules adsorbed in the zeolite channels (**Figure 5*e***).

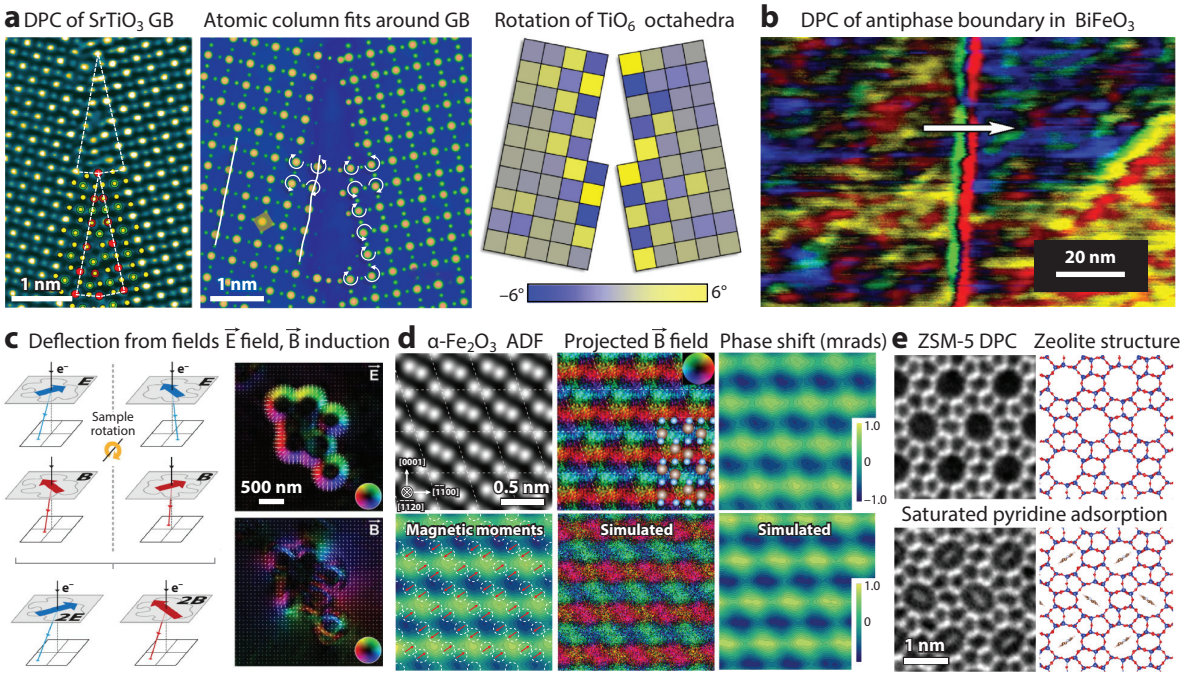

Figure 5

DPC imaging in STEM. (*a*) DPC image and fitted atomic columns of an antiferrodistortive Σ13 GB in $SrTiO_3$. TiO_6 octahedra rotations are measured from the DPC image. Panel adapted with permission from Reference 117; copyright 2021 American Physical Society. (*b*) DPC signal at an antiphase boundary in doped $BiFeO_3$. Panel adapted from Reference 119 (CC BY 4.0). (*c*) Freestanding Ni_2MnGa disks. Panel adapted from Reference 120 with permission from AIP Publishing. (*d*) Structure and magnetic field distribution inside antiferromagnetic α-Fe_2O_3 compared with simulations. Panel adapted from Reference 121 with permission from Springer Nature. (*e*) DPC image and structure of zeolite ZSM-5 with and without adsorbed pyridine molecules. Panel adapted from Reference 118 with permission from Springer Nature. Abbreviations: ADF, annular dark field; DPC, differential phase contrast; GB, grain boundary; STEM, scanning transmission electron micrography.

As mentioned above, DPC imaging is sensitive to any electromagnetic field. However, extreme care must be taken when attempting to measure free electric fields in regions of a sample where the potential is not constant. This is because any change in the local atomic structure will lead to deflection of the STEM probe and thus a DPC signal. **Figure 5*b*** shows the DPC signal measured at an antiphase boundary in doped $BiFeO_3$ by MacLaren et al. (119). The authors concluded that the shifts observed at the boundary are due to the local structural change at the interface and the corresponding change in density rather than originating from a free electric field, and they cautioned that many previous DPC shifts ascribed to electric fields may instead be due to diffraction effects associated with local changes in density, crystallographic orientation, specimen thickness, or polarization. Nevertheless, it is possible to quantitatively measure electric fields if care is taken in both the measurement and interpretation.

Figure 5*c* shows a schematic from Campanini et al. (120) of electron beam deflection in the presence of fields and how rotating the sample 180° can be used to separate the contributions from the electric and magnetic fields. They have performed this experiment on freestanding Ni_2MnGa disks, producing maps of the electrostatic field and magnetic induction vectors. As noted above, the electric field contributions all arise from changes in the specimen thickness, while the magnetic flux lines extend both inside and outside of the sample. **Figure 5*d*** shows magnetic DPC

imaging pushed to the limit by measuring the magnetic field distribution inside antiferromagnetic α-Fe_2O_3 and comparing the results with simulations. To measure these fields with very small magnitudes, they needed to use a magnetic field–free objective lens, carefully subtract the electric field contributions, and use unit-cell averaging with a very high electron dose (121).

3. DIFFRACTION AND 4D-STEM

Electron diffraction patterns contain a large amount of information about the local sample structure. As described above, most STEM imaging methods measure portions of the diffracted electron beam intensity in the far-field region as a function of the probe position. A STEM measurement can be thought of as performing a selected area diffraction (SAD) experiment where the selected area is the portion of the sample covered by the probe's intensity distribution. Many early STEM researchers recognized that STEM diffraction patterns were extremely information rich and that by tuning the STEM probe size and step size between adjacent measurements, materials could be fully characterized by performing many such diffraction measurements in parallel. However, because electron detectors were slow and microscopy had not yet become a digital science with the advent of modern computers, most of these studies were limited to analyzing a small number of diffraction patterns.

The introduction of direct electron detectors dramatically expanded the possibilities for STEM diffraction experiments (22). These detectors can now record full diffraction patterns at frame rates approaching 100,000 images per second, allowing the STEM probe to be moved on the $\approx$10-μs time scale as is typical for the imaging experiments described in the previous section. Because these measurements record a full 2D diffraction pattern over a 2D grid of probe positions, they produce a 4D data set, giving these experiments their general name of 4D-STEM (20). There are two direct electron detector technologies widely used for 4D-STEM studies. The first is an active pixel sensor (APS) detector, which uses semiconductor chips with a sensitive doped epitaxial layer to generate many low-energy electrons, which are recorded via diffusion to sensor diodes, when high-energy electrons pass through APS detectors that are fast, highly sensitive, and possess a large number of pixels, but when integrating the total collected charge, they have poor dynamic range and a wide energy spread per electron (122). One method to improve the resolution and energy spread is to use electron counting to identify single-electron events, but this requires using a very low electron flux or high frame rate to prevent overlapping electron events (123) or hybrid integration-counting processing of the diffraction patterns (124). The other popular class of direct electron cameras is a hybrid pixel array detector consisting of a 2D array of photodiodes bump bonded to an integrated circuit. These detectors typically have very high sensitivity and dynamic range but a smaller number of pixels (2). MacLaren et al. (3) have reviewed detector developments in STEM, and Ophus (22) has reviewed the development and applications of 4D-STEM.

3.1. Convergent Beam Electron Diffraction

The primary difference between conventional SAD and STEM diffraction is that in SAD, the illumination is typically made as parallel as possible, while in STEM a larger probe convergence angle (known as the numerical aperture in optics) is used in order to focus a small probe on the sample surface (19). If the convergence angle is larger than the reciprocal lattice vector of a crystalline sample, the diffracted Bragg disks will overlap and produce an interference pattern. These measurements are known as CBED measurements. CBED can be used to perform local strain and orientation measurements by analyzing the fine details of the diffraction patterns. These analyses typically require detailed calculations or simulations in order to interpret the results.

CBED is a very flexible measurement method, as the diffraction imaging condition can be changed below the sample to allow measurement with convergence angles larger than the Bragg

scattering angle. By recording the different tilt directions serially, Koch (125) has shown that one can record large-angle rocking-beam electron diffraction patterns at even larger convergence angles, which can then be used to solve for both residual aberrations and 3D crystal diffraction patterns. Another CBED technique is to average the diffraction patterns from multiple probe positions, a method known as PACBED (126). Because PACBED measurements integrate out the contrast variations of a small probe being scanned over a unit cell, they can be used to measure material properties such as thickness, tilt, polarization, disorder, and composition with high precision (127, 128). Although CBED patterns contain a wealth of information, it can be difficult to disentangle the origins of various signals. Recent efforts in machine learning have helped in the analysis of diffraction pattern; for example, Pennington et al. (129) have shown that 3D information can be recovered from CBED patterns, while Xu & LeBeau (130) have applied machine learning to PACBED.

3.2. Ronchigrams

If the convergence angle of the STEM probe is increased further or the condenser aperture is removed altogether, a highly defocused diffraction pattern will produce a distorted shadow image of the specimen. These images contain information about electron wave aberrations in electron diffraction, and by recording multiple Ronchigrams from a specimen with different defocus values or sample translations, one can measure the lens aberrations to facilitate hardware aberration correction. For an introduction and demonstration of Ronchigram measurements, readers are referred to the manuscript by Schnitzer et al. (131) and the Ronchigram website (**https://ronchigram.com/**).

3.3. Diffraction from Crystalline Materials

As discussed previously, CBED experiments where the probe convergence angle is larger than the Bragg scattering vectors will produce complex interference patterns in areas where the diffracted disks overlap. If we instead use a convergence angle small enough to avoid overlapping regions, the diffraction patterns become far simpler to interpret, consisting of nearly flat disks representing the sample's diffraction pattern convolved with the reciprocal-space probe shape. This simple interpretation is possible because the STEM probe is larger than the crystalline unit cell and thus does not change as a function of position relative to the unit cell. These experiments are often referred to as NBED (132) or SEND data sets (124). NBED experiments can be used to characterize the local phase of a sample by matching the diffraction pattern to a given crystal structure and orientation. These experiments are typically referred to as automated crystal orientation mapping (ACOM) and usually consist of precomputing a diffraction pattern library over a range of orientations and determining the orientation(s) with the highest correlation to the library. ACOM is often combined with precession electron diffraction (PED), where the beam is continuously rotated around a cone of projection angles in order to produce more interpretable diffraction patterns (133). **Figure 6*a*** shows an example of orientation mapping along a GeS nanowire axis where Sutter et al. (134) used the slowly changing orientation to determine the continuously twisting structure of the nanowire layers. NBED mapping of orientations, grains, and phases has been used to characterize a wide range of crystalline materials (e.g., 46, 135). Coherent phase contrast in the diffracted disks has also been used to measure the strain and rotations between layers of twisted bilayer graphene using a method named Bragg interferometry (136).

Another common NBED application measures local deformation in a crystalline grain by fitting a lattice to the Bragg disks in the diffraction pattern, producing a strain map. NBED has also been used by Ding et al. (139) to estimate oxygen vacancy concentration from in situ strain maps

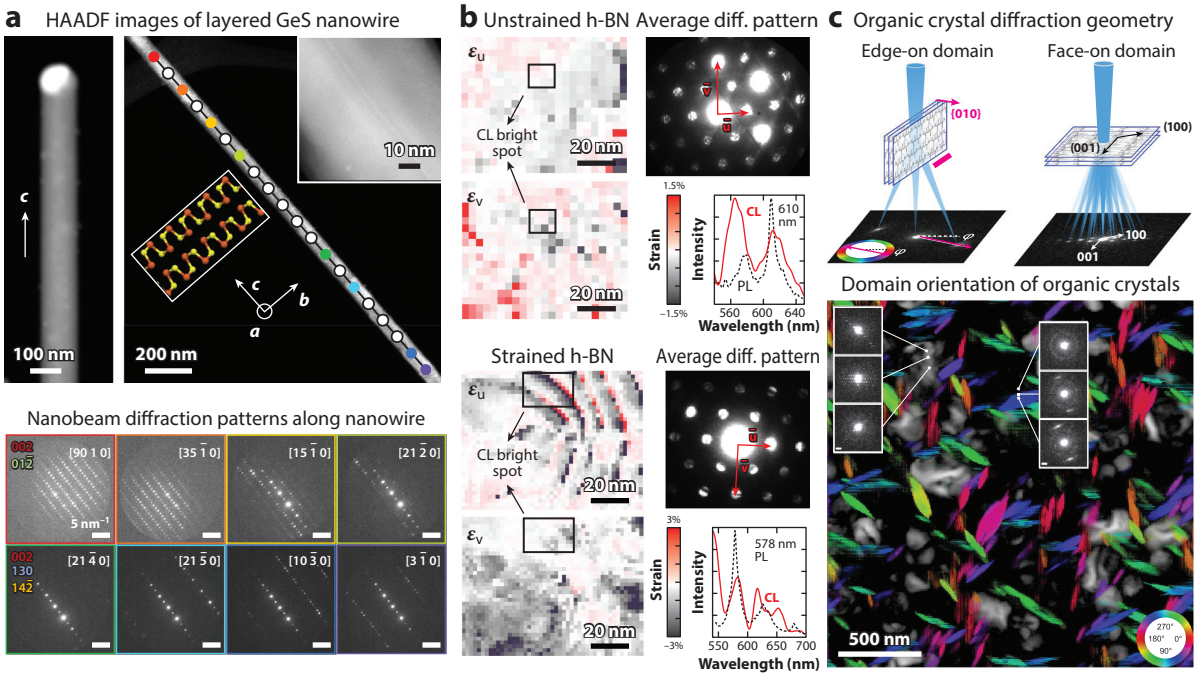

Figure 6

Nanobeam electron diffraction for crystalline materials. (*a*) HAADF images and nanobeam diffraction patterns from a GeS nanowire, showing the lattice twist and diffraction tilt along the nanowire axis. Panel adapted from Reference 134 with permission from Springer Nature. (*b*) Correlation of PL and CL emission with local strain in h-BN. Panel adapted from Reference 137 with permission from Springer Nature. (*c*) Orientation mapping of organic crystals using 4D-SCED. Panel adapted from Reference 138 (CC BY 4.0). Abbreviations: CL, cathodoluminescence; HAADF, high-angle annular dark field; h-BN, hexagonal boron nitride; PL, photoluminescence; SCED, scanning confocal electron diffraction.

of CeO_2. NBED measurements are often complicated by multiple scattering of the electron beam, which produces unwanted contrast in the diffracted Bragg disks (140). One method to reduce these systematic errors is to combine PED with strain mapping (141) while another is to use patterned apertures to improve probe position measurement precision (13). NBED strain mapping can be combined with other measurements to determine structure–property relationships. An example of this is shown in **Figure 6*b***, where Hayee et al. (137) correlated the photoluminescence (PL) and CL response from h-BN to the local lattice strain. They found that deformed lattice regions were associated with the PL and CL signals, but strain was not a requirement for emission.

Measuring the structure of beam-sensitive materials such as polymers or organic molecular materials is a challenge for electron microscopy. Many of these materials are crystalline or semicrystalline but cannot tolerate the electron dose required for imaging the lattices at atomic or near-atomic resolution (84, 86). NBED, however, can characterize these beam-sensitive organic crystals by lowering the electron dose and spreading out the electron probe, using large step sizes between probes and cryogenic cooling (142). Modern detector technology allows us to map the orientation of beam-sensitive organic materials (143). One difficulty with extremely beam-sensitive materials is the long tail of a conventional Airy disk STEM probe, which can damage the sample before the probe reaches the next position. Wu et al. (138) have demonstrated that by using 4D scanning confocal electron diffraction (4D-SCED), the shape of the probe on the sample surface becomes a circular pencil beam, while in diffraction space, the Bragg peaks

become sharper. **Figure 6*c*** shows 4D-SCED measurements of the bulk heterojunction thin film of DRCN5T:$PC_{71}BM$ organic crystals with a low-enough dose to characterize the nucleation and growth of grains during in situ annealing. They found that these organic crystals can nucleate with both face-on and edge-on orientations.

3.4. Diffraction from Amorphous Materials

Many important materials are partially or fully disordered. These amorphous or glassy materials are challenging to study with both intermediate- and atomic-resolution STEM imaging because the complex disordered atomic clusters in samples with even moderate thickness will overlap in projection. Imaging of even primarily crystalline samples can be significantly more difficult if they contain amorphous surface layers. An alternative to studying amorphous materials with imaging is to use electron diffraction. When the convergence angle is very small, the electron probe in real space becomes large enough to sample a sizable volume of the sample, producing patterns similar to traditional electron diffraction experiments yet still retaining some spatial resolution (142). The fundamental structural characteristic of amorphous materials is the lack of long-range ordering; that is, the structural units of the material do not repeat with translation. This lack of translation symmetry can be directly observed in diffraction experiments where the patterns become radially symmetric and form the characteristic broad rings known as amorphous halos. These features in the diffraction pattern are due to the structure factor oscillations of the sample, which act as a fingerprint for the short-range order of the material. Through computational analysis, we can measure the radial distribution function (RDF) of an amorphous material from these patterns (144). The primary advantage of electron diffraction over X-ray diffraction is improved spatial resolution, while the primary disadvantage is that multiple scattering of the electron beam can strongly modulate RDF measurements, which can necessitate using very thin samples to obtain quantitative results.

Treacy & Borisenko (145) have shown that RDF signals are not necessarily unique representations of an amorphous material. This is in part due to averaging over a large atomic volume; thus one method to measure more local information is to use a larger probe convergence angle to produce a smaller probe in real space. STEM experiments measured with large convergence angles produce significantly more variance in diffraction patterns between adjacent probe positions and are usually referred to as fluctuation electron microscopy (FEM) (146). The so-called speckles in the diffraction pattern can be quantified as a function of probe size and scattering angle to determine the degree of medium-range order in a given material (145). If the sample is thin enough, FEM experiments can be used to characterize atomic clusters using atomic-scale probes, a method known as angstrom-beam electron diffraction (147). The angular correlations in FEM patterns can be used to measure icosahedral, octahedral, tetrahedral, and other atomic neighbor shell configurations (148). Cockayne (149) has reviewed the use of electron diffraction to study amorphous materials.

3.5. Diffractive Imaging with Ptychography

As described above, phase contrast imaging with DPC is more dose efficient than incoherent methods such as HAADF, and DPC has higher sensitivity to light elements than BF or ABF. However, converting the complex signal produced by a converged electron probe diffracting from a sample to a two-element momentum vector drops a significant amount of measured information. These diffraction patterns contain scattered intensities from a wide range of spatial frequencies, which can be measured with a pixelated direct electron detector in a 4D-STEM experiment. With many measurements of probes that overlap on the sample surface, we can use direct or iterative computational methods to reconstruct both the complex probe and object wave functions

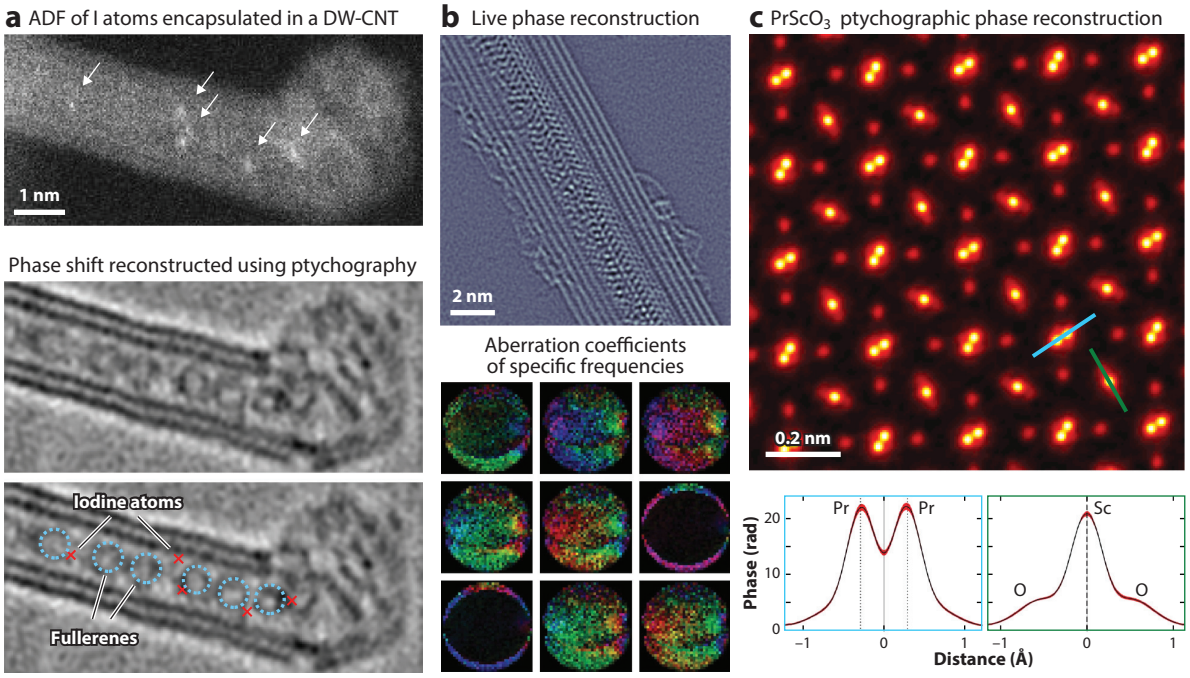

Figure 7

Electron ptychography in STEM. (*a*) Simultaneous ADF and ptychographic reconstruction of I atoms and fullerenes encapsulated in a DW-CNT. Panel adapted from Reference 152 (CC BY 4.0). (*b*) Real-time ptychographic phase reconstruction of a TaTe nanowire encapsulated in a MW-CNT, with live aberration tuning. Panel adapted with permission from Reference 153; copyright 2021 IEEE. (*c*) Multislice ptychographic phase reconstruction of $PrScO_3$, with Pr–Pr and O–Sc–O line traces shown below. Panel adapted from Reference 154 with permission from AAAS. Abbreviations: ADF, annular dark field; DW-CNT, double-walled carbon nanotube; MW-CNT, multiwalled carbon nanotube; STEM, scanning transmission electron microscopy.

in a method known as ptychography. Noniterative reconstruction methods for ptychographic reconstruction are typically faster than iterative methods but also less accurate. Inverse multislice ptychographic reconstruction algorithms can further improve the accuracy and provide some 3D information but require even longer calculation times and must be regularized for stability (150).

Ptychography was first demonstrated by Rodenburg and colleagues (151), who phased Bragg diffraction vectors to images with resolution beyond the diffraction limit. Since then, the structures of various materials have been imaged using ptychography; for example, Yang et al. (152) studied fullerenes and I atoms encapsulated by a double-walled carbon nanotube (DW-CNT), as shown in **Figure 7*a***. The nanotube structure is quite blurry in the accompanying ADF image, but the isolated I atoms are well resolved due to their higher atomic number. The fullene structures are not visible in the ADF image but can be clearly seen in the ptychographic reconstruction. Additionally, the nanotube walls are much better resolved in the ptychographic image, demonstrating the high efficiency of STEM phase contrast imaging. The noniterative ptychographic reconstruction method they used is known as the single side band (SSB) method (152). The SSB method is fast enough to be employed for live phase contrast imaging, such as the image of a TaTe nanowire encapsulated in a multiwalled carbon nanotube, as shown in **Figure 7*b*** and reconstructed by Pelz et al. (153). By examining the reconstructed phase of the strongest spatial frequencies in the data set, Pelz et al. were able to solve and correct for the residual aberrations using an interactive method.

Iterative ptychographic reconstruction can be used to substantially increase the resolution of the reconstructed object waves. Humphry et al. (155) demonstrated experimentally using scanning electron microscopy (SEM) that ptychography could be used to reconstruct the phase of scattering vectors at higher angles than the probe convergence semiangle, that is, beyond the conventional diffraction limit. Jiang et al. (156) showed that applying these concepts to STEM ptychography could push the resolution beyond the ≈0.5-Å limit of incoherent STEM by imaging MoS_2 at 0.39-Å resolution. By performing inverse multislice and mixed-state ptychographic reconstructions, Chen et al. (154) were able to image $PrScO_3$, as shown in **Figure 7*c***, with such high resolution that the blurring of atomic columns was limited only by thermal vibrations. They also demonstrated that depth sectioning of their reconstructions could reveal individual dopants and that inverse multislice ptychography allows for much thicker specimens to be reconstructed. Ptychography is a very useful operating mode in STEM, especially for samples that are beam sensitive or contain light elements, and is becoming more common in atomic-resolution material characterization.

3.6. Other 4D-STEM Methods

STEM diffraction experiments can be modified in a number of ways. One method is to customize the incident wave function of the electron probe by using optical elements in the probe-forming aperture. These include patterned amplitude plates to improve the precision of Bragg disk position measurements (13). Another 4D-STEM amplitude plate experiment is multibeam electron diffraction (MBED), where multiple holes are placed in a binary mask to produce multiple simultaneous electron beams that intersect the sample at different projection angles (157). MBED is essentially a fixed projection angle version of PED where the beam is continuously tilted around a cone of projection angles (133). Phase plates can also be used to produce vortex STEM probes (8), approximately linear phase contrast transfer functions (9, 10), or multiple beams for STEM holography (12) and to correct probe aberrations (11) or add phase diversity to ptychographic reconstructions (158). Some STEM experiments use nonstandard optical setups such as a confocal configuration, which can be used to measure 3D sample information (159), to measure the intensity distribution of STEM probes in real space (160), or to characterize inelastic scattering (161). 4D-SCED has recently been extended to orientation mapping of beam-sensitive organic samples (138).

4. SPECTROSCOPY

A STEM probe passing through a sample can transfer energy through various scattering pathways. The energy spectrum of the vibrational or electronic transitions excited by these scattering events can provide insight into the structure and properties of the material being probed. We can measure these spectra either directly by measuring the energy distribution of the electron beam after passing through a sample or indirectly from photons, auger electrons, or secondary electrons generated by beam–sample interactions. The most common forms of spectroscopy in STEM are EELS (24), XEDS [also known as energy-dispersive X-ray spectrometry (EDXS), which in turn is often shortened to EDS], or energy-dispersive X-ray spectroscopy (26). The flexibility of STEM instruments has also given rise to several other spectroscopic techniques, which are not reviewed here. These include CL, reviewed by Kociak & Zagonel (27), and secondary electron or backscattered electron imaging as a function of detector bias (162). STEM-EELS and XEDS have both benefited enormously from the widespread availability of aberration correction, highly coherent electron beams such as cold field emission sources, and better monochromator and spectrometer hardware (5). EELS methods have been reviewed in the classic book by Egerton (24).

4.1. Electron Energy Loss Spectroscopy

EELS is an incredibly powerful characterization method as it spans energy scales including phonons (≈0.1 eV), band gaps (0.5–6.0 eV), surface plasmons (≈1–5 eV), bulk plasmons (tens of electron volts), and core-loss excitations (from tens to thousands of electron volts). There are many recent improvements in EELS hardware, including in overall instrument design, electron sources, monochromators, aberration correction, electron spectrometer design, and direct electron detectors (163). These advances have improved the energy resolution, spatial resolution, stability, signal-to-noise ratio, and field-of-view size of EELS experiments by leaps and bounds. A widespread application of STEM-EELS in materials science is composition mapping using core-loss EELS edges of the constituent elements. **Figure 8*a*** shows composition mapping of liquid–solid interfaces in a lithium-metal battery sample, imaged at cryogenic temperatures by Zachman et al. (164). They directly observed two distinct dendrite morphologies on the lithium anode, one of which they proposed leads to capacity degradation. Core-loss EELS can also be used to detect very small changes in composition. For example, Yang et al. (165) measured the excess signal in the C K-edge to observe excess gaseous CO on an Au nanoprism in an environmental STEM-EELS experiment, as shown in **Figure 8*b***. They used simulations and modeling to show that the active catalytic sites are located at the highest amplitude points for localized surface plasmons and favorable adsorption sites on the nanoprism structures.

Figure 8*c* shows EELS measurements from Baldi et al. (166) of the plasmon peaks associated with the phase transitions of a single Pd nanocube driven by H adsorption. By observing individual NPs, they showed that the Pd phase transitions were very sharp and were controlled by particle size and surface effects. These results from individual nanostructures emphasize the power of STEM-EELS measurements as compared with ensemble measurements, which would show a broad transition when characterizing a large population simultaneously. EELS sensitivity is now good enough to characterize the spectrum from individual atoms, such as the measurements of single La atoms inside $CaTiO_3$ by Varela et al. (171). Bosman et al. (172) first demonstrated atomic-resolution chemical mapping in EELS, which was followed up by many atomic-resolution EELS studies of various materials.

One of the most fundamental emergent properties of a material is its distribution of allowed atomic vibrational waves and how the density and energies of these phonons depend on the local atomic structure. STEM-EELS provides a unique window into these atomic-scale processes, as demonstrated by the momentum mapping of monolayer graphene by Senga et al. (167), shown in **Figure 8*d***. The researchers used density-functional perturbation theory to simulate these spectra, which showed excellent agreement with the experimental maps. This experiment demonstrated the feasibility of performing momentum-energy measurements at very high resolution, perhaps limited only by the delocalization of the excitation being studied. **Figure 8*e*** shows the spatial distributions of EELS measurements performed by Yan et al. (168) of phonon modes across a stacking fault in SiC. The researchers measured a large change in phonon excitation intensity as well as a redshift of the acoustic vibration modes. This result demonstrates the feasibility of studying thermal transport in materials with extremely high spatial resolution.

Figure 8*f* demonstrates how EELS could be used to probe electronic orbitals. Bugnet et al. (169) have spatially mapped the antibonding π^* and σ^8 orbitals of individual graphene layers in graphite, sandwiched between Bi_2Se_3 and SiC. They validated these observations with quantitative inelastic channeling simulations, where both the inelastic and elastic scattering of the STEM beam are accounted for. STEM-EELS can also probe very small variations in core-loss energies, such as the measurements by Sheen et al. (170) of the N K-edge in InGaN quantum wells,

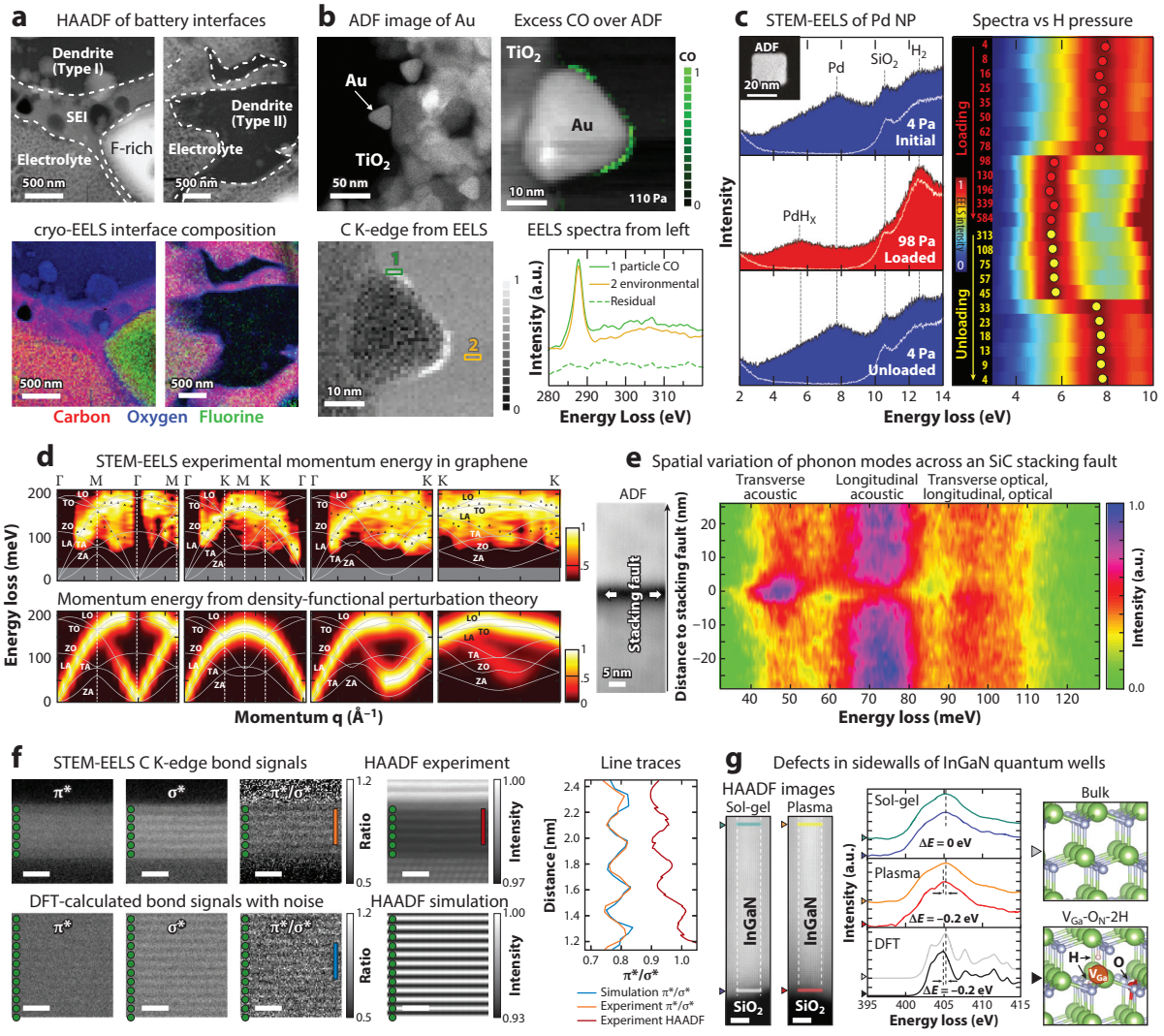

Figure 8

EELS in STEM. (*a*) EELS composition mapping of liquid–solid interfaces in a lithium-metal battery at cryogenic temperatures. Panel adapted from Reference 164 with permission from Springer Nature. (*b*) Excess CO adsorption on Au nanoprism edges measured with core-loss EELS. Panel adapted from Reference 165 with permission from Springer Nature. (*c*) H adsorption and desorption from Pd nanocubes measured from bulk plasmon EELS signals. Panel adapted from Reference 166 with permission from Springer Nature. (*d*) EELS measurements and density-functional perturbation theory simulations of energy-momentum maps from monolayer graphene. Panel adapted from Reference 167 with permission from Springer Nature. (*e*) Phonon modes measured using EELS as a function of distance to a stacking fault in Si. Panel adapted with permission from Reference 168. (*f*) Spatial distribution of excited electronic states corresponding to in-plane (σ*) and out-of-plane (π*) bonds in graphene, measured with EELS and compared with DFT and electron scattering simulations. Scale bars represent 1 nm. Panel adapted from Reference 169 (CC BY 4.0). (*g*) EELS spectra from bulk and surface regions in InGaN quantum wells prepared with sol-gel and plasma synthesis routes compared with DFT calculations of bulk and $V_{Ga}O_N$-2H defect complex. Scale bars represent 2 nm. Panel adapted with permission from Reference 170. Abbreviations: ADF, annular dark field; DFT, density-functional theory; EELS, electron energy loss spectroscopy; HAADF, high-angle ADF; NP, nanoparticle; SEI, solid–electrolyte interphase; STEM, scanning transmission electron microscopy.

shown in **Figure 8*g***. They compared sol-gel and plasma-enhanced atomic layer deposition (ALD) synthesis methods for these samples, and, by using DFT modeling, they determined that the spectral differences were due to the presence of V_{Ga}–O_N–2H point defects on the GaN sidewalls in the plasma-enhanced ALD sample. These observations have direct ramifications for producing blue nanoscale light-emitting diodes based on InGaN quantum wells with low defect concentrations.

4.2. X-Ray Energy-Dispersive Spectroscopy

The first instrument created to measure electron beam–generated X-rays was developed by Castaing (173) and could perform XEDS without spatial resolution. High-voltage STEM has the advantage of a much smaller interaction volume than SEM and therefore much higher spatial resolution in chemical maps. However the X-ray signals generated are also much smaller in magnitude, which, when combined with the poor detection efficiency of early X-ray detectors, necessitated higher brightness sources and large solid angle detectors to reliably produce chemical signals higher than the background. After the development of aberration correction, atomic-resolution XEDS was soon accomplished (174).

Quantitative composition analysis in XEDS requires that the measured signals be scaled by ratios, colloquially known as k-factors, to account for low X-ray detection efficiency and instrument- and sample-specific measurement limitations. Estimating the k-factors with first principles modeling is possible, but often leads to large systematic errors, and both absorption due to sample thickness and signal modulation due to sample orientation require careful treatment. Achieving high accuracy typically requires experimental calibration measurements from pure phases on a given instrument. To overcome these limitations, Watanabe & Williams (175) introduced the ζ-factor method based on the previous treatment for absorption. The ζ-factor method requires only pure element reference phases, gives the absolute composition, and has other quantification advantages. The main limitation compared with simple k-factors is the requirement to independently measure specimen thickness and beam current. XEDS simulations can be performed using the methods given by Allen & Findlay (71), which may be required to correct for the crystal-zone axis channeling of the electron beam. Watanabe and colleagues (26, 176) have reviewed XEDS experimental methods.

5. 3D TOMOGRAPHY

We live in 3D space, and many materials science samples contain complex variation in three dimensions. However, the vast majority of STEM experiments essentially measure 2D projections. STEM samples are typically thinned as far as possible, but even thin single-crystal materials still possess vacuum-sample interfaces at their surfaces along the beam direction. Thus, most STEM experiments provide minimal or no information about sample variation along the beam direction, a concept formalized by the projection-slice theorem. There is, however, a simple method in STEM to recover 3D information: record data at multiple projection directions. These tomography experiments range from analyzing stereo pairs over a small or large tilt range, to recording many projection directions over a tilt range spanning up to 180°, to performing ex situ or even in situ experiments where many projection directions are recorded from a sample over multiple time points during a structural transformation. Kübel et al. (177) have reviewed STEM tomography in detail, Miao et al. (28) have reviewed atomic-resolution electron tomography, Hata et al. (178) have reviewed applications of diffraction-contrast STEM and deformation characterization tomography in materials science, and Wang et al. (30) have reviewed electron tomography of catalyst NPs. Wolf et al. (179) have examined the possibilities for using STEM tomography in biological imaging.

5.1. Stereo Pair Imaging

For structures with a small spatial extent in two or three dimensions, two images can uniquely determine how they are positioned in 3D space. This includes 1D point defects such as dopant atoms, vacancies, or small inclusions and 2D line defects such as dislocations. A larger angular separation of the two images will give improved depth resolution, but for samples that contain many overlapping defect structures, the 3D geometry may still be ambiguous. In microscopy research, this imaging method is typically referred to as stereoscopic imaging, stereoscopy, or stereo pairs of images. STEM stereo pair imaging has been used to image a variety of defects, and stereo pair 3D reconstructions from 4D-STEM data sets have recently been demonstrated by Ganeeva et al. (180). Despite stereo pair experiments being easier to perform and reconstruct in three dimensions, most modern 3D STEM studies use many more images and tomographic reconstruction in order to reconstruct complex 3D structures.

5.2. Intermediate-Resolution Tomography

As discussed in the previous sections, STEM imaging is preferred for most materials science samples in part because it produces much more robust contrast for thick samples. This is important for tomographic measurements, since tilting a flat TEM foil away from the surface normal direction will increase the projected thickness. In particular, HAADF-STEM has found widespread application in STEM tomography, as these measurements contain little or no phase contrast and are closest to obeying the linear projection assumption required for quantitative tomographic reconstruction, at least when considering the integrated signal. Note, however, that HAADF imaging will still produce a decaying signal for thicker sample regions, which in turn produces nonlinear reconstructed intensities. Van den Broek et al. (181) and Zhong et al. (182) have discussed this artifact and how to correct it.

Tomographic volumes can also be reconstructed from spectroscopic data sets in order to measure material properties such as composition in three dimensions as opposed to just 3D structure. **Figure 9*a*** shows an example of spectroscopic tomography where Genc et al. (183) reconstructed the composition of battery cathode particles in a 3D volume using XEDS scans as the input. From these reconstructions, they identified Ni surface segregation to the particle surfaces, which they predicted may form a diffusion barrier for Li migration. ADF-STEM is a particularly useful tool for tomographic reconstruction of nanostructures because it produces monotonic, nearly linear contrast with the atomic number of projected thickness. **Figure 9*b*** shows how relatively low-dose STEM tomography was used by Segal-Peretz et al. (184) to measure the 3D structure of a block copolymer sample. From these reconstructions, the authors were able to identify subsurface defects such as splitting of the columns of polystyrene-b-poly(methyl methacrylate) or subsurface merge points that demonstrate different growth rates at the top and bottom regions of the film. The high contrast of ADF-STEM also makes it a prime candidate for in situ experiments. If the transformation being studied proceeds slowly enough, multiple tilt series can be recorded sequentially in order to produce a time-resolved 3D measurement. Vanrompay et al. (185) have performed time-resolved STEM tomography, as shown in **Figure 9*c***, to characterize the annealing response of Au nanostars in three dimensions. The researchers confirmed that the annealing reshaping of the particles is driven by curvature-induced surface diffusion. The authors studied the plasmonic properties of the nanostars as a function of particle shape using numerical boundary-element-method simulations and determined that annealing dramatically reduces the shape-induced electric field enhancement. *Z*-contrast STEM tomography at intermediate resolution has been reviewed by Leary et al. (186).

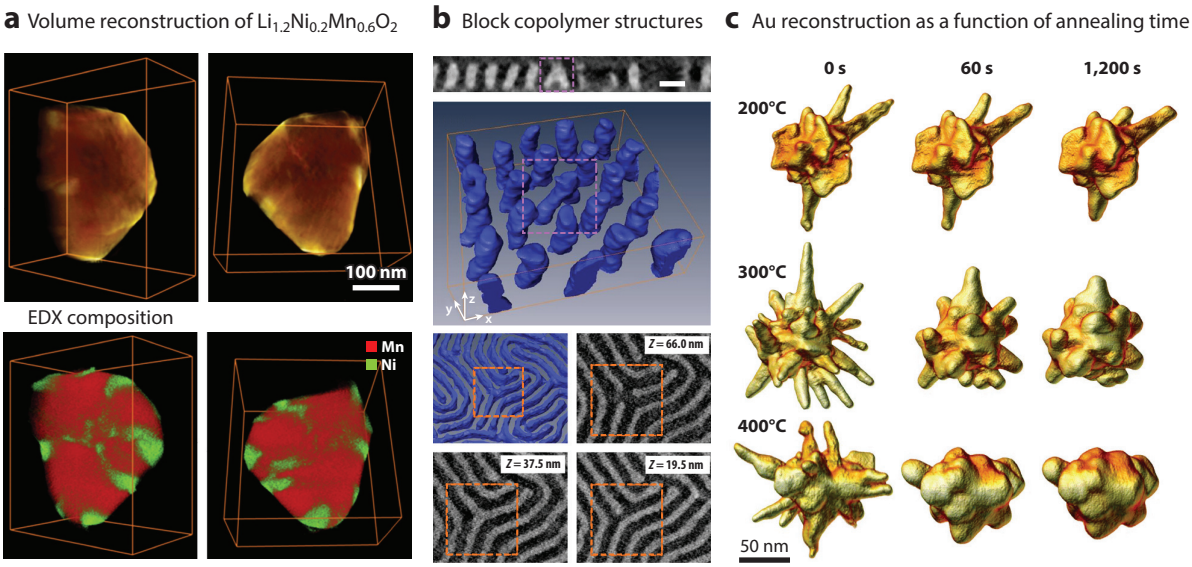

Figure 9

Examples of intermediate-resolution electron tomography. (*a*) Simultaneous HAADF and EDX tomographic 3D reconstructions of battery cathode particles. Panel adapted from Reference 183 with permission from Elsevier. (*b*) The 3D structure block copolymers solved with STEM tomography. The top reconstruction shows a splitting defect, while the bottom shows the structure of a lamellae merge point. Panel adapted with permission from Reference 184; copyright 2015 American Chemical Society. (*c*) The 3D structural evolution of three Au nanostars at three different annealing times, measured with fast in situ tomography. Panel adapted from Reference 185 (CC BY 4.0). Abbreviations: EDX, energy-dispersive X-ray; HAADF, high-angle annular dark field; STEM, scanning transmission electron microscopy; XEDS, X-ray energy-dispersive spectroscopy.

5.3. Atomic Electron Tomography

The ultimate structural characterization for any sample is to determine both the position and species of each individual atom. There are currently only two characterization methods with sufficient spatial resolution to approach this ideal: atom probe tomography (APT) and atomic electron tomography (AET). These methods are complementary in materials science. APT is destructive, has a lower spatial resolution than AET, and will miss recording some fraction of the atoms. However, it can be used for much larger sample volumes than AET and has significantly better inherent chemical sensitivity. APT has been reviewed by Gault et al. (187) and others and is not discussed further in this review.

The first experimental development toward AET was performed by Van Aert et al. (188), who reconstructed the 3D structure of an Ag NP embedded in an Al matrix by estimating the number of atoms in each column from two HAADF-STEM images aligned to zone axes separated by 45°. Their approach was similar to the stereo pair examples discussed above, but due to overlapping atomic signals, their reconstruction was nonunique and required assuming prior knowledge of the crystal structure. To achieve a more robust AET reconstruction, Goris et al. (189) combined an intermediate-resolution tomographic reconstruction with atomic-resolution images captured along four zone axes, which they then overlaid onto the lower-resolution reconstruction. One of their reconstructions of an Au nanorod is shown in **Figure 10*a*** with sufficient resolution to identify surface facets of different nanorods and to compute a 3D strain tensor. Another step toward AET was made by Scott et al. (190), who performed a full atomic-resolution tilt series of a decahedral Au NP. Their following AET study of a decahedral Pd NP, where they were

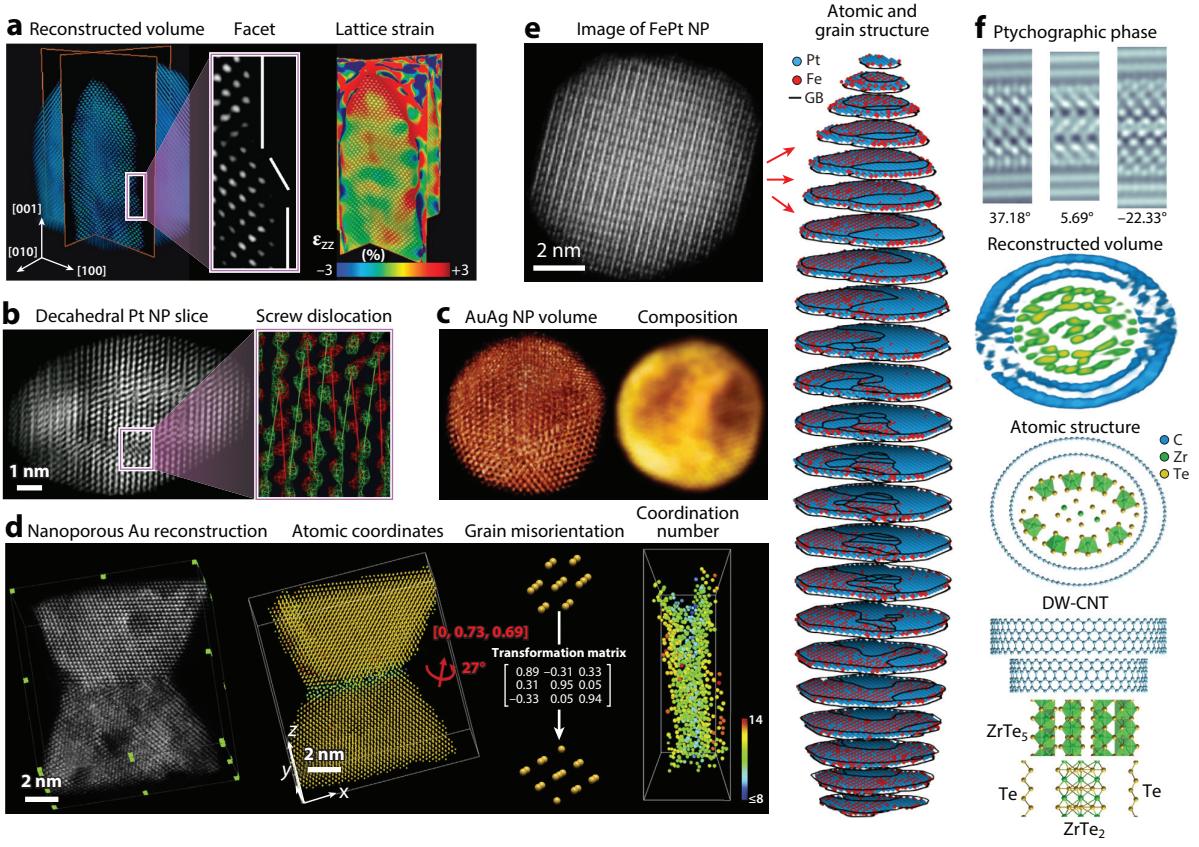

Figure 10

Examples of atomic-resolution electron tomography. (*a*) Reconstruction of an Au nanorod showing surface facets and internal strain. Panel adapted from Reference 189 with permission from Springer Nature. (*b*) Slice from a volume reconstruction of a multiply twinned Pt NP showing an internal screw dislocation. Panel adapted with permission from Reference 191. (*c*) Structure of an AuAg nanocluster showing the reconstructed volume and composition, where darker regions show two Ag-rich cores. Panel adapted from Reference 192 (CC BY 4.0). (*d*) Reconstruction and atomic structure of a GB in nanoporous gold, where the relative grain misorientation and coordinate number of atoms in the boundary are shown. Panel adapted with permission from Reference 193. (*e*) Atomic positions and species of all atoms in an FePt NP, with internal GBs shown. Panel adapted with permission from Reference 194. (*f*) Ptychographic imaging of a ZrTe nanowire consisting of multiple phases, encapsulated in a DW-CNT, with reconstructed volume and atomic structures plotted. Panel adapted with permission from Reference 195. Abbreviations: DW-CNT, double-walled carbon nanotube; GB, grain boundary; NP, nanoparticle.

able to directly map the 3D atomic structure of a screw dislocation (191), is shown in **Figure 10*b***. Haberfehlner et al. (192) performed atomic-resolution tomography of AgAu NPs, with an example shown in **Figure 10*c***, where the approximate composition was validated with XEDS and EELS. Both of these studies had a high enough resolution to determine most of the surface and internal structure of the NPs but not all individual atoms.

The measurement of the 3D position of all atoms in a sample was first demonstrated by Xu et al. (196), who solved the atomic structure of a W tip sample. They found that the sample was strained by the introduction of interstitial carbon, but they were not able to directly image C atoms because the HAADF-STEM imaging method used was not sensitive to light elements. Yang et al. (194) next performed an AET experiment on an FePt NP, which is shown in **Figure 10*e***. They were able to determine the species of all atomic sites and thereby map the complex internal face-centered

cubic $L1_0$, and $L1_2$ grain structures in the FePt NP. Another milestone in material research was achieved by Wang et al. (193), who used AET to characterize a GB in nanoporous Au. Their reconstruction of 3D atomic coordinates is shown in **Figure 10*d*** and represents the structural equivalent of the chemical GBs characterized in **Figure 10*e***.

AET performed with HAADF-STEM has now proven to be able to measure atomic positions for samples that can tolerate high electron doses, and it can distinguish different atomic species if the atomic numbers are different enough. One of the next frontiers for AET will be to implement modalities such as phase contrast imaging that are more dose efficient and able to image light elements. Pelz et al. (195) have experimentally demonstrated ptychographic AET, which they used to solve the structure of a complex ZrTe nanowire encapsulated in a DW-CNT, shown in **Figure 10*f***. Pushing phase contrast methods to thicker specimens will require including multiple scattering in the reconstruction algorithm. This has been theoretically investigated at atomic resolution using plane-wave phase contrast TEM imaging (197) and shown experimentally at near-atomic resolution (198). As discussed above, ptychography is capable of depth sectioning, and multiple scattering can be included in the phase reconstruction (154); such a reconstruction could be performed jointly with the 3D tomographic reconstruction to maximize 3D information transfer (199). Another future avenue for improving AET is to fuse information from multiple measurement channels, such as combining HAADF with ptychography or using XEDS or EELS to better determine the atomic species present (200).

6. CONCLUSION AND FUTURE PROSPECTS

This review highlights recent STEM studies that have included quantitative imaging, diffraction, spectroscopy, and tomography. It focuses on the wide breadth of measurements possible in STEM and the use of computational methods for the quantification of structure and material properties. Open source software tools for direct microscope control, analysis, and simulation of imaging, diffraction, spectroscopy, and tomography experiments will be essential for STEM to reach its true potential. The combination of open source tools and FAIR data principles will also both dramatically improve the reproducibility of STEM and make it easier for newcomers to electron microscopy to learn best practices for extremely complex experiments, especially those recording high-dimensional data sets or those that perform multimodal analysis. Another growth area for STEM experiments is time-resolved in situ experiments, which multiply all of the previously discussed analysis requirements by the number of time points recorded. The benefits outweigh the cost, however, as in situ experiments unlock the ability to study dynamic processes in materials, potentially in more realistic operating environments. Finally, I note that to truly close the feedback loop between experiment and theory, we must build semi- or fully automated experimental platforms for data collection, extraction, and analysis, which themselves optimize the experimental parameters and select features of interest. Machine learning offers the most promising route toward implementing these autonomous platforms in addition to the already large impact it is having on materials science and microscopy research.

DISCLOSURE STATEMENT

The author is not aware of any affiliations, memberships, funding, or financial holdings that might be perceived as affecting the objectivity of this review.

ACKNOWLEDGMENTS

I thank Holly Barton, Steven Zeltmann, and Stephanie Ribet for helpful suggestions proofreading this manuscript. C.O. acknowledges support from the Department of Energy Early

Career Research Award program. Work at the Molecular Foundry was supported by the Office of Science, Office of Basic Energy Sciences, of the US Department of Energy under contract DE-AC02-05CH11231.

LITERATURE CITED

1. Mullarkey T, Downing C, Jones L. 2021. Development of a practicable digital pulse read-out for dark-field STEM. *Microsc. Microanal.* 27(1):99–108
2. Tate MW, Purohit P, Chamberlain D, Nguyen KX, Hovden R, et al. 2016. High dynamic range pixel array detector for scanning transmission electron microscopy. *Microsc. Microanal.* 22(1):237–49
3. MacLaren I, Macgregor TA, Allen CS, Kirkland AI. 2020. Detectors—the ongoing revolution in scanning transmission electron microscopy and why this important to material characterization. *Apl. Mater.* 8(11):110901
4. Nord M, Webster RW, Paton KA, McVitie S, McGrouther D, et al. 2020. Fast pixelated detectors in scanning transmission electron microscopy. Part I: data acquisition, live processing, and storage. *Microsc. Microanal.* 26(4):653–66
5. Krivanek OL, Dellby N, Hachtel JA, Idrobo JC, Hotz M, et al. 2019. Progress in ultrahigh energy resolution EELS. *Ultramicroscopy* 203:60–67
6. Sawada H, Tomita T, Naruse M, Honda T, Hambridge P, et al. 2005. Experimental evaluation of a spherical aberration-corrected TEM and STEM. *Microscopy* 54(2):119–21
7. Kimoto K. 2014. Practical aspects of monochromators developed for transmission electron microscopy. *J. Electron Microsc.* 63(5):337–44
8. McMorran BJ, Agrawal A, Anderson IM, Herzing AA, Lezec HJ, et al. 2011. Electron vortex beams with high quanta of orbital angular momentum. *Science* 331(6014):192–95
9. Ophus C, Ciston J, Pierce J, Harvey TR, Chess J, et al. 2016. Efficient linear phase contrast in scanning transmission electron microscopy with matched illumination and detector interferometry. *Nat. Commun.* 7:10719
10. Yang H, Ercius P, Nellist PD, Ophus C. 2016. Enhanced phase contrast transfer using ptychography combined with a pre-specimen phase plate in a scanning transmission electron microscope. *Ultramicroscopy* 171:117–25
11. Verbeeck J, Béché A, Müller-Caspary K, Guzzinati G, Luong MA, Den Hertog M. 2018. Demonstration of a 2 × 2 programmable phase plate for electrons. *Ultramicroscopy* 190:58–65
12. Harvey TR, Yasin FS, Chess JJ, Pierce JS, dos Reis RMS, et al. 2018. Interpretable and efficient interferometric contrast in scanning transmission electron microscopy with a diffraction-grating beam splitter. *Phys. Rev. Appl.* 10(6):061001
13. Zeltmann SE, Müller A, Bustillo KC, Savitzky B, Hughes L, et al. 2020. Patterned probes for high precision 4D-STEM Bragg measurements. *Ultramicroscopy* 209:112890
14. Reed BW, Moghadam A, Bloom R, Park S, Monterrosa A, et al. 2019. Electrostatic subframing and compressive-sensing video in transmission electron microscopy. *Struct. Dyn.* 6(5):054303
15. Brown L. 1997. A synchrotron in a microscope. In *Electron Microscopy and Analysis 1997, Proceedings of the Institute of Physics Electron Microscopy and Analysis Group Conference, University of Cambridge, 2–5 September 1997*, ed. JM Rodenberg, pp. 17–22. Boca Raton, FL: CRC Press
16. Ramasse QM. 2017. Twenty years after: how "aberration correction in the STEM" truly placed a "a synchrotron in a microscope." *Ultramicroscopy* 180:41–51
17. Liu JJ. 2021. Advances and applications of atomic-resolution scanning transmission electron microscopy. *Microsc. Microanal.* 27(5):943–95
18. De Graef M. 2003. *Introduction to Conventional Transmission Electron Microscopy*. Cambridge, UK: Cambridge Univ. Press
19. Pennycook SJ, Nellist PD. 2011. *Scanning Transmission Electron Microscopy: Imaging and Analysis*. New York: Springer
20. Ophus C, Ercius P, Sarahan M, Czarnik C, Ciston J. 2014. Recording and using 4D-STEM datasets in materials science. *Microsc. Microanal.* 20(S3):62–63

21. Spence J, Zuo J. 2013. *Electron Microdiffraction*. New York: Springer
22. Ophus C. 2019. Four-dimensional scanning transmission electron microscopy (4D-STEM): from scanning nanodiffraction to ptychography and beyond. *Microsc. Microanal.* 25(3):563–82
23. Swanson L, Schwind G. 2009. A review of the cold-field electron cathode. *Adv. Imaging Electron Phys.* 159:63–100
24. Egerton RF. 2011. *Electron Energy-Loss Spectroscopy in the Electron Microscope*. New York: Springer
25. Ikeno H, Mizoguchi T. 2017. Basics and applications of ELNES calculations. *Microscopy* 66(5):305–27
26. Watanabe M. 2011. X-ray energy-dispersive spectrometry in scanning transmission electron microscopes. In *Scanning Transmission Electron Microscopy: Imaging and Analysis*, ed. SJ Pennycook, PD Nellist, pp. 291–351. New York: Springer
27. Kociak M, Zagonel L. 2017. Cathodoluminescence in the scanning transmission electron microscope. *Ultramicroscopy* 176:112–31
28. Miao J, Ercius P, Billinge SJ. 2016. Atomic electron tomography: 3D structures without crystals. *Science* 353(6306):aaf2157
29. Elbaum M. 2018. Quantitative cryo-scanning transmission electron microscopy of biological materials. *Adv. Mater.* 30(41):1706681
30. Wang Z, Ke X, Sui M. 2022. Recent progress on revealing 3D structure of electrocatalysts using advanced 3D electron tomography: a mini review. *Front. Chem.* 10:872117
31. Olszta M, Hopkins D, Fiedler KR, Oostrom M, Akers S, Spurgeon SR. 2022. An automated scanning transmission electron microscope guided by sparse data analytics. *Microsc. Microanal.* 28(5):1611–21
32. Feng J, Somlyo AP, Somlyo AV, Shao Z. 2007. Automated electron tomography with scanning transmission electron microscopy. *J. Microsc.* 228(3):406–12
33. Savitzky BH, Zeltmann SE, Hughes LA, Brown HG, Zhao S, et al. 2021. py4DSTEM: a software package for four-dimensional scanning transmission electron microscopy data analysis. *Microsc. Microanal.* 27(4):712–43
34. Spurgeon SR, Ophus C, Jones L, Petford-Long A, Kalinin SV, et al. 2021. Towards data-driven next-generation transmission electron microscopy. *Nat. Mater.* 20(3):274–79
35. Wilkinson MD, Dumontier M, Aalbersberg IJ, Appleton G, Axton M, et al. 2016. The FAIR guiding principles for scientific data management and stewardship. *Sci. Data* 3(1):160018
36. Kalinin SV, Ophus C, Voyles PM, Erni R, Kepaptsoglou D, et al. 2022. Machine learning in scanning transmission electron microscopy. *Nat. Rev. Methods Primers* 2(1):11
37. Hovden R, Cueva P, Mundy JA, Muller DA. 2013. The open-source Cornell Spectrum Imager. *Microsc. Today* 21(1):40–44
38. de la Pema F, Prestat E, Fauske VT, Burdet P, Lahnemann J, et al. 2022. hyperspy/hyperspy: Release v1.7.3. *Zenodo*. **https://doi.org/10.5281/zenodo.7263263**
39. Nord M, Vullum PE, MacLaren I, Tybell T, Holmestad R. 2017. Atomap: a new software tool for the automated analysis of atomic resolution images using two-dimensional Gaussian fitting. *Adv. Struct. Chem. Imaging* 3(1):9
40. O'Connell EN, Moore K, McFall E, Hennessy M, Moynihan E, et al. 2022. TopoTEM: A python package for quantifying and visualizing scanning transmission electron microscopy data of polar topologies. *Microsc. Microanal.* 28(4):1444–52
41. Slater T, CameronGBell, Mohsen. 2021. ePSIC-DLS/ParticleSpy: v0.5.2 *Zenodo*. **https://zenodo.org/record/4668722/export/hx#.ZEmYF3bMKUk**
42. Cautaerts N, Crout P, Ånes HW, Prestat E, Jeong J, et al. 2022. Free, flexible and fast: orientation mapping using the multi-core and GPU-accelerated template matching capabilities in the python-based open source 4D-STEM analysis toolbox Pyxem. *Ultramicroscopy* 237:113517
43. Crout P, Johnstone DN, Hogas S, Martineau B, isabelwood100, et al. 2021. pyxem/diffsims: diffsims 0.4.2 *Zenodo*. **https://doi.org/10.5281/zenodo.4697299**
44. Johnstone DN, Martineau BH, Crout P, Midgley PA, Eggeman AS. 2020. Density-based clustering of crystal (mis) orientations and the *orix* Python library. *J. Appl. Crystallogr.* 53(5):1293–98
45. Clausen A, Weber D, Ruzaeva K, Migunov V, Baburajan A, et al. 2020. LiberTEM: software platform for scalable multidimensional data processing in transmission electron microscopy. *J. Open Source Softw.* 5(50):2006

46. Ophus C, Zeltmann SE, Bruefach A, Rakowski A, Savitzky BH, et al. 2022. Automated crystal orientation mapping in py4DSTEM using sparse correlation matching. *Microsc. Microanal.* 28(2):390–403
47. Mukherjee D, Unocic R. 2020. STEMtooL: an open source Python toolkit for analyzing electron microscopy datasets. *Microsc. Microanal.* 26(S2):2960–62
48. Somnath S, Smith CR, Laanait N, Vasudevan RK, Jesse S. 2019. USID and pycroscopy – open source frameworks for storing and analyzing imaging and spectroscopy data. *Microsc. Microanal.* 25(S2):220–21
49. Ziatdinov M, Ghosh A, Wong T, Kalinin SV. 2021. AtomAI: a deep learning framework for analysis of image and spectroscopy data in (scanning) transmission electron microscopy and beyond. arXiv:2105.07485 [physics.data-an]
50. Gürsoy D, De Carlo F, Xiao X, Jacobsen C. 2014. TomoPY: a framework for the analysis of synchrotron tomographic data. *J. Synchrotron Radiat.* 21(5):1188–93
51. van Aarle W, Palenstijn WJ, De Beenhouwer J, Altantzis T, Bals S, et al. 2015. The ASTRA toolbox: a platform for advanced algorithm development in electron tomography. *Ultramicroscopy* 157:35–47
52. Hanwell MD, Harris CJ, Genova A, Schwartz J, Jiang Y, Hovden R. 2019. Tomviz: open source platform connecting image processing pipelines to GPU accelerated 3D visualization. *Microsc. Microanal.* 25(S2):408–9
53. Kremer JR, Mastronarde DN, McIntosh JR. 1996. Computer visualization of three-dimensional image data using IMOD. *J. Struct. Biol.* 116(1):71–76
54. Schaffer B. 2016. Digital micrograph. In *Transmission Electron Microscopy: Diffraction, Imaging, and Spectrometry*, ed. CB Carter, DB Williams, pp. 167–96. Cham, Switz.: Springer
55. Jones L, Yang H, Pennycook TJ, Marshall MS, Van Aert S, et al. 2015. Smart Align—a new tool for robust non-rigid registration of scanning microscope data. *Adv. Struct. Chem. Imaging* 1(1):8
56. Ophus C, Ciston J, Nelson CT. 2016. Correcting nonlinear drift distortion of scanning probe and scanning transmission electron microscopies from image pairs with orthogonal scan directions. *Ultramicroscopy* 162:1–9
57. Savitzky BH, El Baggari I, Clement CB, Waite E, Goodge BH, et al. 2018. Image registration of low signal-to-noise cryo-STEM data. *Ultramicroscopy* 191:56–65
58. Berkels B, Liebscher CH. 2019. Joint non-rigid image registration and reconstruction for quantitative atomic resolution scanning transmission electron microscopy. *Ultramicroscopy* 198:49–57
59. Bárcena-González G, de la Paz Guerrero-Lebrero M, Guerrero E, Yañez A, Nuñez-Moraleda B, et al. 2020. CDrift: an algorithm to correct linear drift from a single high-resolution STEM image. *Microsc. Microanal.* 26(5):913–20
60. Kirkland EJ. 2020. *Advanced Computing in Electron Microscopy*. Cham, Switz.: Springer. 3rd ed.
61. Cowley JM, Moodie AF. 1957. The scattering of electrons by atoms and crystals. I. A new theoretical approach. *Acta Crystallogr.* 10(10):609–19
62. Pelz PM, Rakowski A, DaCosta LR, Savitzky BH, Scott MC, Ophus C. 2021. A fast algorithm for scanning transmission electron microscopy imaging and 4D-STEM diffraction simulations. *Microsc. Microanal.* 27(4):835–48
63. Lobato I, Van Dyck D. 2014. An accurate parameterization for scattering factors, electron densities and electrostatic potentials for neutral atoms that obey all physical constraints. *Acta Crystallogr. A Found. Adv.* 70(6):636–49
64. Mendis BG. 2018. *Electron Beam-Specimen Interactions and Simulation Methods in Microscopy*. Hoboken, NJ: Wiley & Sons
65. Madsen J, Susi T. 2021. The abTEM code: transmission electron microscopy from first principles. *Open Res. Eur.* 1:24
66. Barthel J, Cattaneo M, Mendis BG, Findlay SD, Allen LJ. 2020. Angular dependence of fast-electron scattering from materials. *Phys. Rev. B* 101(18):184109
67. Rossouw D, Botton GA. 2013. Plasmonic response of bent silver nanowires for nanophotonic subwavelength waveguiding. *Phys. Rev. Lett.* 110(6):066801
68. Hébert C, Luitz J, Schattschneider P. 2003. Improvement of energy loss near edge structure calculation using Wien2k. *Micron* 34(3–5):219–25
69. Brown HG, Ciston J, Ophus C. 2019. Linear-scaling algorithm for rapid computation of inelastic transitions in the presence of multiple electron scattering. *Phys. Rev. Res.* 1(3):033186

70. Rangel DaCosta L, Brown HG, Pelz PM, Rakowski A, Barber N, et al. 2021. Prismatic 2.0 – simulation software for scanning and high resolution transmission electron microscopy (STEM and HRTEM). *Micron* 151:103141
71. Allen LJ, Findlay S. 2015. Modelling the inelastic scattering of fast electrons. *Ultramicroscopy* 151:11–22
72. Lobato I, Van Dyck D. 2015. MULTEM: A new multislice program to perform accurate and fast electron diffraction and imaging simulations using graphics processing units with CUDA. *Ultramicroscopy* 156:9–17
73. Barthel J. 2018. Dr. Probe: a software for high-resolution STEM image simulation. *Ultramicroscopy* 193:1–11
74. Forbes B, Martin A, Findlay S, D'alfonso A, Allen L. 2010. Quantum mechanical model for phonon excitation in electron diffraction and imaging using a Born-Oppenheimer approximation. *Phys. Rev. B* 82(10):104103
75. Pryor A, Ophus C, Miao J. 2017. A streaming multi-GPU implementation of image simulation algorithms for scanning transmission electron microscopy. *Adv. Struct. Chem. Imaging* 3(1):15
76. Ophus C. 2017. A fast image simulation algorithm for scanning transmission electron microscopy. *Adv. Struct. Chem. Imaging* 3(1):13
77. Mendis B. 2019. An inelastic multislice simulation method incorporating plasmon energy losses. *Ultramicroscopy* 206:112816
78. Dwyer C. 2005. Multislice theory of fast electron scattering incorporating atomic inner-shell ionization. *Ultramicroscopy* 104(2):141–51
79. Zeiger PM, Rusz J. 2020. Efficient and versatile model for vibrational STEM-EELS. *Phys. Rev. Lett.* 124(2):025501
80. Lugg N, Kothleitner G, Shibata N, Ikuhara Y. 2015. On the quantitativeness of EDS STEM. *Ultramicroscopy* 151:150–59
81. Chen Z, Taplin D, Weyland M, Allen LJ, Findlay S. 2017. Composition measurement in substitutionally disordered materials by atomic resolution energy dispersive x-ray spectroscopy in scanning transmission electron microscopy. *Ultramicroscopy* 176:52–62
82. Yamamoto N, Araya K, Toda A, Sugiyama H. 2001. Light emission from surfaces, thin films and particles induced by high-energy electron beam. *Surface Interface Anal.* 31(2):79–86
83. Schaffer M, Schaffer B, Ramasse Q. 2012. Sample preparation for atomic-resolution STEM at low voltages by FIB. *Ultramicroscopy* 114:62–71
84. Egerton R, Watanabe M. 2022. Spatial resolution in transmission electron microscopy. *Micron* 160:103304
85. Zhang Z, Wang W, Dong Z, Yang X, Liang F, et al. 2022. The trends of in situ focused ion beam technology: toward preparing transmission electron microscopy lamella and devices at the atomic scale. *Adv. Electron. Mater.* 8(9):2101401
86. Egerton R. 2019. Radiation damage to organic and inorganic specimens in the TEM. *Micron* 119:72–87
87. Velazco A, Béché A, Jannis D, Verbeeck J. 2022. Reducing electron beam damage through alternative STEM scanning strategies, part I: experimental findings. *Ultramicroscopy* 232:113398
88. Kuei B, Gomez ED. 2021. Pushing the limits of high-resolution polymer microscopy using antioxidants. *Nat. Commun.* 12(1):153
89. Kuipers J, Kalicharan RD, Wolters AH, van Ham TJ, Giepmans BN. 2016. Large-scale scanning transmission electron microscopy (nanotomy) of healthy and injured zebrafish brain. *JoVE* (111):e53635
90. Ke X, Zhang M, Zhao K, Su D. 2022. Moiré fringe method via scanning transmission electron microscopy. *Small Methods* 6(1):2101040
91. Gauquelin N, Van den Bos K, Béché A, Krause F, Lobato I, et al. 2017. Determining oxygen relaxations at an interface: a comparative study between transmission electron microscopy techniques. *Ultramicroscopy* 181:178–90
92. Treacy MM. 2011. *Z* dependence of electron scattering by single atoms into annular dark-field detectors. *Microsc. Microanal.* 17(6):847–58
93. Crewe AV, Wall J, Langmore J. 1970. Visibility of single atoms. *Science* 168(3937):1338–40
94. Singhal A, Yang J, Gibson J. 1997. STEM-based mass spectroscopy of supported Re clusters. *Ultramicroscopy* 67(1–4):191–206

95. Voyles P, Muller D, Kirkland E. 2004. Depth-dependent imaging of individual dopant atoms in silicon. *Microsc. Microanal.* 10(2):291–300
96. Allen JE, Hemesath ER, Perea DE, Lensch-Falk JL, Li Z, et al. 2008. High-resolution detection of Au catalyst atoms in Si nanowires. *Nat. Nanotechnol.* 3(3):168–73
97. Colliex C, Gloter A, March K, Mory C, Stéphan O, et al. 2012. Capturing the signature of single atoms with the tiny probe of a STEM. *Ultramicroscopy* 123:80–89
98. Rosenauer A, Gries K, Müller K, Pretorius A, Schowalter M, et al. 2009. Measurement of specimen thickness and composition in $Al_xGa_{1-x}N$/GaN using high-angle annular dark field images. *Ultramicroscopy* 109(9):1171–82
99. Krivanek OL, Chisholm MF, Nicolosi V, Pennycook TJ, Corbin GJ, et al. 2010. Atom-by-atom structural and chemical analysis by annular dark-field electron microscopy. *Nature* 464(7288):571–74
100. Yankovich AB, Berkels B, Dahmen W, Binev P, Sanchez SI, et al. 2014. Picometre-precision analysis of scanning transmission electron microscopy images of platinum nanocatalysts. *Nat. Commun.* 5:4155
101. De Backer A, Martinez G, MacArthur K, Jones L, Béché A, et al. 2015. Dose limited reliability of quantitative annular dark field scanning transmission electron microscopy for nano-particle atom-counting. *Ultramicroscopy* 151:56–61
102. Zou YC, Mogg L, Clark N, Bacaksiz C, Milovanovic S, et al. 2021. Ion exchange in atomically thin clays and micas. *Nat. Mater.* 20(12):1677–82
103. Luo K, Liu B, Hu W, Dong X, Wang Y, et al. 2022. Coherent interfaces govern direct transformation from graphite to diamond. *Nature* 607(7919):486–91
104. LeBeau JM, Findlay SD, Allen LJ, Stemmer S. 2008. Quantitative atomic resolution scanning transmission electron microscopy. *Phys. Rev. Lett.* 100(20):206101
105. Hartel P, Rose H, Dinges C. 1996. Conditions and reasons for incoherent imaging in STEM. *Ultramicroscopy* 63(2):93–114
106. Shi F, Li F, Ma Y, Zheng F, Feng R, et al. 2019. In situ transmission electron microscopy study of nanocrystal formation for electrocatalysis. *ChemNanoMat* 5(12):1439–55
107. LeBeau JM, D'Alfonso AJ, Findlay SD, Stemmer S, Allen LJ. 2009. Quantitative comparisons of contrast in experimental and simulated bright-field scanning transmission electron microscopy images. *Phys. Rev. B* 80(17):174106
108. Okunishi E, Ishikawa I, Sawada H, Hosokawa F, Hori M, Kondo Y. 2009. Visualization of light elements at ultrahigh resolution by STEM annular bright field microscopy. *Microsc. Microanal.* 15(S2):164–65
109. Ishikawa R, Okunishi E, Sawada H, Kondo Y, Hosokawa F, Abe E. 2011. Direct imaging of hydrogen-atom columns in a crystal by annular bright-field electron microscopy. *Nat. Mater.* 10(4):278–81
110. Byeon P, Hong Y, Bae HB, Shin J, Choi JW, Chung S-Y. 2021. Atomic-scale unveiling of multiphase evolution during hydrated Zn-ion insertion in vanadium oxide. *Nat. Commun.* 12(1):4599
111. Findlay SD, Saito T, Shibata N, Sato Y, Matsuda J, et al. 2010. Direct imaging of hydrogen within a crystalline environment. *Appl. Phys. Express* 3(11):116603
112. Dekkers N, De Lang H. 1974. Differential phase contrast in a STEM. *Optik* 41(4):452–56
113. Rose H. 1977. Nonstandard imaging methods in electron microscopy. *Ultramicroscopy* 2:251–67
114. Lubk A, Zweck J. 2015. Differential phase contrast: an integral perspective. *Phys. Rev. A* 91(2):023805
115. Lazić I, Bosch EG, Lazar S. 2016. Phase contrast STEM for thin samples: integrated differential phase contrast. *Ultramicroscopy* 160:265–80
116. Shibata N, Findlay SD, Kohno Y, Sawada H, Kondo Y, Ikuhara Y. 2012. Differential phase-contrast microscopy at atomic resolution. *Nat. Phys.* 8(8):611–15
117. Han B, Zhu R, Li X, Wu M, Ishikawa R, et al. 2021. Two-dimensional room-temperature giant antiferrodistortive $SrTiO_3$ at a grain boundary. *Phys. Rev. Lett.* 126(22):225702
118. Shen B, Wang H, Xiong H, Chen X, Bosch EG, et al. 2022. Atomic imaging of zeolite-confined single molecules by electron microscopy. *Nature* 607(7920):703–7
119. MacLaren I, Wang L, McGrouther D, Craven AJ, McVitie S, et al. 2015. On the origin of differential phase contrast at a locally charged and globally charge-compensated domain boundary in a polar-ordered material. *Ultramicroscopy* 154:57–63
120. Campanini M, Nasi L, Albertini F, Erni R. 2020. Disentangling nanoscale electric and magnetic fields by time-reversal operation in differential phase-contrast STEM. *Appl. Phys. Lett.* 117(15):154102

121. Kohno Y, Seki T, Findlay SD, Ikuhara Y, Shibata N. 2022. Real-space visualization of intrinsic magnetic fields of an antiferromagnet. *Nature* 602(7896):234–39
122. McMullan G, Faruqi A, Clare D, Henderson R. 2014. Comparison of optimal performance at 300 keV of three direct electron detectors for use in low dose electron microscopy. *Ultramicroscopy* 147:156–63
123. Li X, Zheng SQ, Egami K, Agard DA, Cheng Y. 2013. Influence of electron dose rate on electron counting images recorded with the K2 camera. *J. Struct. Biol.* 184(2):251–60
124. Gallagher-Jones M, Ophus C, Bustillo KC, Boyer DR, Panova O, et al. 2019. Nanoscale mosaicity revealed in peptide microcrystals by scanning electron nanodiffraction. *Commun. Biol.* 2:26
125. Koch CT. 2011. Aberration-compensated large-angle rocking-beam electron diffraction. *Ultramicroscopy* 111(7):828–40
126. LeBeau JM, Findlay SD, Wang X, Jacobson AJ, Allen LJ, Stemmer S. 2009. High-angle scattering of fast electrons from crystals containing heavy elements: simulation and experiment. *Phys. Rev. B* 79(21):214110
127. LeBeau JM, D'Alfonso AJ, Wright NJ, Allen LJ, Stemmer S. 2011. Determining ferroelectric polarity at the nanoscale. *Appl. Phys. Lett.* 98(5):052904
128. Ophus C, Ercius P, Huijben M, Ciston J. 2017. Non-spectroscopic composition measurements of $SrTiO_3$-$La_{0.7}Sr_{0.3}MnO_3$ multilayers using scanning convergent beam electron diffraction. *Appl. Phys. Lett.* 110(6):063102
129. Pennington RS, Van den Broek W, Koch CT. 2014. Third-dimension information retrieval from a single convergent-beam transmission electron diffraction pattern using an artificial neural network. *Phys. Rev. B* 89(20):205409
130. Xu W, LeBeau JM. 2018. A deep convolutional neural network to analyze position averaged convergent beam electron diffraction patterns. *Ultramicroscopy* 188:59–69
131. Schnitzer N, Sung SH, Hovden R. 2019. Introduction to the Ronchigram and its calculation with Ronchigram.com. *Microsc. Today* 27(3):12–15
132. Liu Z, Zhang Q, Qin LC. 2005. Accurate determination of atomic structure of multiwalled carbon nanotubes by nondestructive nanobeam electron diffraction. *Appl. Phys. Lett.* 86(19):191903
133. Rauch E, Véron M. 2014. Automated crystal orientation and phase mapping in TEM. *Mater. Charact.* 98:1–9
134. Sutter P, Wimer S, Sutter E. 2019. Chiral twisted van der Waals nanowires. *Nature* 570(7761):354–57
135. Eggeman AS, Krakow R, Midgley PA. 2015. Scanning precession electron tomography for three-dimensional nanoscale orientation imaging and crystallographic analysis. *Nat. Commun.* 6:7267
136. Kazmierczak NP, Van Winkle M, Ophus C, Bustillo KC, Carr S, et al. 2021. Strain fields in twisted bilayer graphene. *Nat. Mater.* 20(7):956–63
137. Hayee F, Yu L, Zhang JL, Ciccarino CJ, Nguyen M, et al. 2020. Revealing multiple classes of stable quantum emitters in hexagonal boron nitride with correlated optical and electron microscopy. *Nat. Mater.* 19(5):534–39
138. Wu M, Harreiß C, Ophus C, Johnson M, Fink RH, Spiecker E. 2022. Seeing structural evolution of organic molecular nano-crystallites using 4D scanning confocal electron diffraction (4D-SCED). *Nat. Commun.* 13(1):2911
139. Ding Y, Choi Y, Chen Y, Pradel KC, Liu M, Wang ZL. 2020. Quantitative nanoscale tracking of oxygen vacancy diffusion inside single ceria grains by in situ transmission electron microscopy. *Mater. Today* 38:24–34
140. Pekin TC, Gammer C, Ciston J, Minor AM, Ophus C. 2017. Optimizing disk registration algorithms for nanobeam electron diffraction strain mapping. *Ultramicroscopy* 176:170–76
141. Rouviere JL, Béché A, Martin Y, Denneulin T, Cooper D. 2013. Improved strain precision with high spatial resolution using nanobeam precession electron diffraction. *Appl. Phys. Lett.* 103(24):241913
142. Bustillo KC, Zeltmann SE, Chen M, Donohue J, Ciston J, et al. 2021. 4D-STEM of beam-sensitive materials. *Acc. Chem. Res.* 54(11):2543–51
143. Panova O, Ophus C, Takacs CJ, Bustillo KC, Balhorn L, et al. 2019. Diffraction imaging of nanocrystalline structures in organic semiconductor molecular thin films. *Nat. Mater.* 18(8):860–65
144. Mu X, Wang D, Feng T, Kübel C. 2016. Radial distribution function imaging by STEM diffraction: phase mapping and analysis of heterogeneous nanostructured glasses. *Ultramicroscopy* 168:1–6

145. Treacy M, Borisenko K. 2012. The local structure of amorphous silicon. *Science* 335(6071):950–53
146. Voyles P, Muller D. 2002. Fluctuation microscopy in the STEM. *Ultramicroscopy* 93(2):147–59
147. Lu Z, Lu AKA, Zhang F, Tian Y, Jiang J, et al. 2021. Crystal-like order stabilizing glasses: Structural origin of ultra-stable metallic glasses. arXiv:2111.02606 [cond-mat.dis-nn]
148. Liu A, Neish M, Stokol G, Buckley G, Smillie L, et al. 2013. Systematic mapping of icosahedral short-range order in a melt-spun $Zr_{36}Cu_{64}$ metallic glass. *Phys. Rev. Lett.* 110(20):205505
149. Cockayne DJ. 2007. The study of nanovolumes of amorphous materials using electron scattering. *Annu. Rev. Mater. Res.* 37:159–87
150. Schloz M, Pekin TC, Chen Z, Van den Broek W, Muller DA, Koch CT. 2020. Overcoming information reduced data and experimentally uncertain parameters in ptychography with regularized optimization. *Opt. Express* 28(19):28306–23
151. Nellist P, McCallum B, Rodenburg JM. 1995. Resolution beyond the 'information limit' in transmission electron microscopy. *Nature* 374(6523):630–32
152. Yang H, Rutte R, Jones L, Simson M, Sagawa R, et al. 2016. Simultaneous atomic-resolution electron ptychography and *Z*-contrast imaging of light and heavy elements in complex nanostructures. *Nat. Commun.* 7:12532
153. Pelz PM, Johnson I, Ophus C, Ercius P, Scott MC. 2021. Real-time interactive 4D-STEM phase-contrast imaging from electron event representation data: less computation with the right representation. *IEEE Signal Proc. Mag.* 39(1):25–31
154. Chen Z, Jiang Y, Shao YT, Holtz ME, Odstrčil M, et al. 2021. Electron ptychography achieves atomic-resolution limits set by lattice vibrations. *Science* 372(6544):826–31
155. Humphry M, Kraus B, Hurst A, Maiden A, Rodenburg J. 2012. Ptychographic electron microscopy using high-angle dark-field scattering for sub-nanometre resolution imaging. *Nat. Commun.* 3:730
156. Jiang Y, Chen Z, Han Y, Deb P, Gao H, et al. 2018. Electron ptychography of 2D materials to deep sub-ångström resolution. *Nature* 559(7714):343–49
157. Hong X, Zeltmann SE, Savitzky BH, DaCosta LR, Müller A, et al. 2021. Multibeam electron diffraction. *Microsc. Microanal.* 27(1):129–39
158. Pelz PM, Qiu WX, Bücker R, Kassier G, Miller RD. 2017. Low-dose cryo electron ptychography via non-convex bayesian optimization. *Sci. Rep.* 7(1):9883
159. Hashimoto A, Shimojo M, Mitsuishi K, Takeguchi M. 2009. Three-dimensional imaging of carbon nanostructures by scanning confocal electron microscopy. *J. Appl. Phys.* 106(8):086101
160. Etheridge J, Lazar S, Dwyer C, Botton GA. 2011. Imaging high-energy electrons propagating in a crystal. *Phys. Rev. Lett.* 106(16):160802
161. Zheng C, Zhu Y, Lazar S, Etheridge J. 2014. Fast imaging with inelastically scattered electrons by off-axis chromatic confocal electron microscopy. *Phys. Rev. Lett.* 112(16):166101
162. Inada H, Su D, Egerton R, Konno M, Wu L, et al. 2011. Atomic imaging using secondary electrons in a scanning transmission electron microscope: experimental observations and possible mechanisms. *Ultramicroscopy* 111(7):865–76
163. Krivanek OL, Ursin JP, Bacon NJ, Corbin GJ, Dellby N, et al. 2009. High-energy-resolution monochromator for aberration-corrected scanning transmission electron microscopy/electron energy-loss spectroscopy. *Philos. Trans. R. Soc. A* 367(1903):3683–97
164. Zachman MJ, Tu Z, Choudhury S, Archer LA, Kourkoutis LF. 2018. Cryo-STEM mapping of solid–liquid interfaces and dendrites in lithium-metal batteries. *Nature* 560(7718):345–49
165. Yang WCD, Wang C, Fredin LA, Lin PA, Shimomoto L, et al. 2019. Site-selective Co disproportionation mediated by localized surface plasmon resonance excited by electron beam. *Nat. Mater.* 18(6):614–19
166. Baldi A, Narayan TC, Koh AL, Dionne JA. 2014. In situ detection of hydrogen-induced phase transitions in individual palladium nanocrystals. *Nat. Mater.* 13(12):1143–48
167. Senga R, Suenaga K, Barone P, Morishita S, Mauri F, Pichler T. 2019. Position and momentum mapping of vibrations in graphene nanostructures. *Nature* 573(7773):247–50
168. Yan X, Liu C, Gadre CA, Gu L, Aoki T, et al. 2021. Single-defect phonons imaged by electron microscopy. *Nature* 589(7840):65–69

169. Bugnet M, Ederer M, Lazarov V, Li L, Ramasse Q, et al. 2022. Imaging the spatial distribution of electronic states in graphene using electron energy-loss spectroscopy: prospect of orbital mapping. *Phys. Rev. Lett.* 128(11):116401
170. Sheen M, Ko Y, Kim D-U, Kim J, Byun J-H, et al. 2022. Highly efficient blue ingan nanoscale light-emitting diodes. *Nature* 608(7921):56–61
171. Varela M, Findlay S, Lupini A, Christen H, Borisevich A, et al. 2004. Spectroscopic imaging of single atoms within a bulk solid. *Phys. Rev. Lett.* 92(9):095502
172. Bosman M, Keast V, Garcia-Munoz J, D'Alfonso AJ, Findlay S, Allen L. 2007. Two-dimensional mapping of chemical information at atomic resolution. *Phys. Rev. Lett.* 99(8):086102
173. Castaing R. 1951. *Application of electron probes to local chemical and crystallographic analysis.* PhD Thesis, Univ. Paris
174. Watanabe M, Okunishi E, Aoki T. 2010. Atomic-level chemical analysis by EELS and XEDS in aberration-corrected scanning transmission electron microscopy. *Microsc. Microanal.* 16(S2):66–67
175. Watanabe M, Williams D. 1999. The new form of the zeta-factor method for quantitative microanalysis in AEM-XEDS and its evaluation. *Microsc. Microanal.* 5(S2):88–89
176. Watanabe M, Williams D. 2006. The quantitative analysis of thin specimens: a review of progress from the cliff-lorimer to the new ζ-factor methods. *J. Microsc.* 221(2):89–109
177. Kübel C, Voigt A, Schoenmakers R, Otten M, Su D, et al. 2005. Recent advances in electron tomography: TEM and HAADF-STEM tomography for materials science and semiconductor applications. *Microsc. Microanal.* 11(5):378–400
178. Hata S, Furukawa H, Gondo T, Hirakami D, Horii N, et al. 2020. Electron tomography imaging methods with diffraction contrast for materials research. *Microscopy* 69(3):141–55
179. Wolf SG, Shimoni E, Elbaum M, Houben L. 2018. STEM tomography in biology. In *Cellular Imaging*, ed. E Hanssen, pp. 33–60. Cham, Switz.: Springer
180. Ganeeva G, Altingövde O, Khac QO, Stellacci F, Fua P, et al. 2022. Automatic 3D reconstruction by deep learning neural networks using images acquired via 4D-STEM stereo imaging. *Microsc. Microanal.* 28(S1):218–20
181. Van den Broek W, Rosenauer A, Goris B, Martinez G, Bals S, et al. 2012. Correction of non-linear thickness effects in HAADF STEM electron tomography. *Ultramicroscopy* 116:8–12
182. Zhong Z, Aveyard R, Rieger B, Bals S, Palenstijn WJ, Batenburg KJ. 2018. Automatic correction of nonlinear damping effects in HAADF–STEM tomography for nanomaterials of discrete compositions. *Ultramicroscopy* 184:57–65
183. Genc A, Kovarik L, Gu M, Cheng H, Plachinda P, et al. 2013. XEDS STEM tomography for 3D chemical characterization of nanoscale particles. *Ultramicroscopy* 131:24–32
184. Segal-Peretz T, Winterstein J, Doxastakis M, Ramírez-Hernández A, Biswas M, et al. 2015. Characterizing the three-dimensional structure of block copolymers via sequential infiltration synthesis and scanning transmission electron tomography. *ACS Nano* 9(5):5333–47
185. Vanrompay H, Bladt E, Albrecht W, Béché A, Zakhozheva M, et al. 2018. 3D characterization of heat-induced morphological changes of Au nanostars by fast in situ electron tomography. *Nanoscale* 10(48):22792–801
186. Leary R, Midgley PA, Thomas JM. 2012. Recent advances in the application of electron tomography to materials chemistry. *Acc. Chem. Res.* 45(10):1782–91
187. Gault B, Chiaramonti A, Cojocaru-Mirédin O, Stender P, Dubosq R, et al. 2021. Atom probe tomography. *Nat. Rev. Methods Primers* 1(1):51
188. Van Aert S, Batenburg KJ, Rossell MD, Erni R, Van Tendeloo G. 2011. Three-dimensional atomic imaging of crystalline nanoparticles. *Nature* 470(7334):374–77
189. Goris B, Bals S, Van den Broek W, Carbó-Argibay E, Gómez-Graña S, et al. 2012. Atomic-scale determination of surface facets in gold nanorods. *Nat. Mater.* 11(11):930–35
190. Scott M, Chen CC, Mecklenburg M, Zhu C, Xu R, et al. 2012. Electron tomography at 2.4-ångström resolution. *Nature* 483(7390):444–47
191. Chen CC, Zhu C, White ER, Chiu CY, Scott M, et al. 2013. Three-dimensional imaging of dislocations in a nanoparticle at atomic resolution. *Nature* 496(7443):74–77

192. Haberfehlner G, Thaler P, Knez D, Volk A, Hofer F, et al. 2015. Formation of bimetallic clusters in superfluid helium nanodroplets analysed by atomic resolution electron tomography. *Nat. Commun.* 6(1):8779
193. Wang C, Duan H, Chen C, Wu P, Qi D, et al. 2020. Three-dimensional atomic structure of grain boundaries resolved by atomic-resolution electron tomography. *Matter* 3(6):1999–2011
194. Yang Y, Chen CC, Scott M, Ophus C, Xu R, et al. 2017. Deciphering chemical order/disorder and material properties at the single-atom level. *Nature* 542(7639):75–79
195. Pelz PM, Griffin S, Stonemeyer S, Popple D, Devyldere H, et al. 2022. Solving complex nanostructures with ptychographic atomic electron tomography. arXiv:2206.08958 [physics.app-ph]
196. Xu R, Chen CC, Wu L, Scott M, Theis W, et al. 2015. Three-dimensional coordinates of individual atoms in materials revealed by electron tomography. *Nat. Mater.* 14(11):1099–103
197. Ren D, Ophus C, Chen M, Waller L. 2020. A multiple scattering algorithm for three dimensional phase contrast atomic electron tomography. *Ultramicroscopy* 208:112860
198. Whittaker ML, Ren D, Ophus C, Zhang Y, Waller L, et al. 2022. Ion complexation waves emerge at the curved interfaces of layered minerals. *Nat. Commun.* 13(1):3382
199. Lee J, Lee M, Park Y, Ophus C, Yang Y. 2022. Multislice electron tomography using 4D-STEM. arXiv:2210.12636 [cond-mat.mtrl-sci]
200. Schwartz J, Di ZW, Jiang Y, Fielitz AJ, Ha DH, et al. 2022. Imaging atomic-scale chemistry from fused multi-modal electron microscopy. *NPJ Comput. Mater.* 8(1):16

Annual Review of Materials Research

Volume 53, 2023

Contents

Indexes

Errata

An online log of corrections to *Annual Review of Materials Research* articles may be found at http://www.annualreviews.org/errata/matsci